PAPER

Check for updates

Dynamic electroosmotic flow and solute dispersion through a nanochannel filled with an electrolyte surrounded by a layer of a dielectric and immiscible liquid†

Sourav Chowdhury, [ID] [a] Sanjib Kr Pal [ID] [b] and Partha P. Gopmandal [ID] *[a]

The present article deals with the modulation of oscillatory electroosmotic flow (EOF) and solute dispersion across a nanochannel filled with an electrolyte solution surrounded by a layer of a dielectric liquid. The dielectric permittivity of the liquid layer adjacent to supporting rigid walls is taken to be lower than that of the electrolyte solution. Besides, the aforesaid liquid layer may bear additional mobile charges, *e.g.*, free lipid molecules, charged surfactant molecules *etc.*, which in turn lead to a nonzero charge along the liquid–liquid interface. Such a layer of a dielectric liquid resembles the membrane of various biological cells. An AC voltage is applied to generate the fluid motion. Note that among others, the major advantage of AC voltage is that it can suppress the formation of gas bubbles that are often very detrimental in flow through microdevices. Considering the combined impact of ion partitioning and ion steric effects, we have studied the EOF modulation and its impact on the dispersion of the solute band of given width placed initially at the middle of the channel. The full scale numerical results for flow modulation induced by an AC electric field and its impact on the solute transport are presented considering a wide range of pertinent parameters. It is observed that the molar concentration of additional charge present in the dielectric liquid layer and its thickness, interfacial charge, and concentration of the bulk electrolyte, ion partitioning and ion steric effects, frequency of oscillatory electric field, channel height *etc.*, have a substantial impact on the flow modulation, effective dispersion coefficient as well as broadening of the solute band across the channel. We have further highlighted the impact of the Péclet number on the transport and dispersion of solutes. Along with the numerical results, several benchmark analytical results under various limits are deduced for electrostatic potential, flow velocity and various quantities associated with the dispersion process.

1 Introduction

Hydrodynamic dispersion of a solute band placed inside a fluidic channel occurs due to the combined impacts of molecular diffusion and fluid convection. For such cases, an additional convective flux due to the flow velocity is added with the flux due to molecular diffusion, which further intensifies the broadening of the solute band. The dispersion of a solute in the presence of the fluid convection has either favourable or adverse effects depending on the type of the processes.[1]

For example, the dispersion is favourable in the mixing process, which leads to a faster and enhanced mixing of samples with the background liquid medium.[2] In contrast, hydrodynamic dispersion has detrimental effects on the separation process as it reduces the resolution of the analytical separation.[3] Thus, a complete knowledge on the interplay between the fluid convection and the molecular diffusion in the dispersion process is essential to achieve a precise and controlled dispersion of a solute band across fluidic devices that deal with the analytical separation or mixing processes.

Historically, solute dispersion through a circular tube under laminar pressure driven Hagen–Poiseuille flow was studied by Taylor.[4] Shortly after, using the method of moments, Aris obtained the expression for the effective dispersion coefficient of passive solutes, which are generally uncharged or at their isoelectric point.[5,6] Note that the Taylor–Aris dispersion coefficient is often used to determine the material properties, *e.g.*, the molecular diffusion coefficient and the hydrodynamic

[a] *Department of Mathematics, National Institute of Technology Durgapur, Durgapur-713209, India. E-mail: ppgopmandal.maths@nitdgp.ac.in, parthap1218@gmail.com; Tel: +91-7250276690*

[b] *Department of Mathematics, Jadavpur University, Jadavpur-700032, Kolkata, India*

† Electronic supplementary information (ESI) available: Nomenclature, the spatial distribution of the concentration of additional mobile ions present in the dielectric liquid layer and some additional results to support the findings. See DOI: https://doi.org/10.1039/d4sm01255k

radius of solutes.[7] The fundamental mechanism that leads to an enhanced dispersion is the impact of a nonuniform velocity gradient on the molecular diffusion, and thus a stronger velocity gradient may lead to an enhanced dispersion. It is important to note that the Taylor–Aris dispersion coefficient depends on other associated physical parameters but not on the time. Thus, the analysis based on the Taylor–Aris model may be applied only at a long time limit.[8] Such an inherent assumption of the Taylor–Aris model was further relaxed by Gill and Sankarasubramanian.[9] They proposed a general dispersion model which is capable of estimating the dispersion coefficient and the area-averaged concentration of a solute for all values of time. Thereafter, a remarkable advancement in the study of solute dispersion is made by several researchers. Fife and Nicholes studied the dispersion of a solute band across a tube of arbitrary cross section under a time-dependent flow field.[10] The impact of the catalytic wall reaction on the dispersion of passive contaminants through a circular tube under time dependent laminar flow is studied numerically by Mazumder and Das.[11] The transport and dispersion of solutes in open channels was further studied by Ng and Yip using homogenization methods.[12] Ng further studied the dispersion of chemical species through a tube under steady and oscillatory pressure driven flow considering a reversible or an irreversible wall reaction.[13] The dispersion of passive solutes suspended in a liquid flowing through a parallel plate channel under time dependent Couette–Poiseuille flow was studied by Paul and Mazumder.[14] Using a multi-scale perturbation method, Karmakar et al. further analysed the impact of transient Couette–Poiseuille flow on the dispersion of passive contaminants through a porous channel.[15]

All the studies indicated above deal with the dispersion due to nonuniform flow velocity across a channel where the characteristic length scale is exactly the same as that characterizes the cross-sectional geometry. In contrast, for the dispersion process driven by electrokinetic transport of an ionized liquid flowing through microfluidic devices, the length scale is the thickness of the electric double layer (EDL).[16] Besides, it is further difficult to utilize the pressure driven flow for channels with size down to micrometer or even less. Note that an electrokinetic transport phenomenon, e.g., electroosmosis induced by the interaction of an external electric field with the excess counterions present in the EDL. The hydrodynamic dispersion through microfluidic devices due to electroosmosis does not require any movable mechanical part, and thus offers long-term stability as well as ability to achieve a precise control of fluid flow driven by externally applied voltage drop.[17] Compared to the purely pressure driven flow, the electroosmotic flow (EOF) through microdevices with uniform wall charge properties leads to a weaker hydrodynamic dispersion and produces a high device resolution with the same through-put.[18] Thus, the hydrodynamic dispersion due to the EOF is beneficial in designing various tools for analytical separation and detection of samples. In recent years significant attention has been paid to design various microdevices that combine the mechanical and electrical components. The readers are referred to recent articles which paid significant attention to design various electrified lab-on-disc systems, intelligent nano-channels, etc. as well as to study the electrokinetically driven flow across such tiny devices.[19–24] Motivated by this trend, several researchers further studied the hydrodynamic dispersion through microdevices considering the EOF with uniform surface ζ-potential (the key parameter that indicates the electrostatic charge of the supporting walls of the conduits).[25–29] Hoshyargar et al. studied the dispersion of solutes considering the EOF of viscoelastic fluids within a slit microchannel.[30] Existing studies indicate that a substantial dispersion of a solute band interacting with the EOF through microdevices is further possible. The same can be done by modifying the geometry of microdevices and/or by considering spatially varying the ζ-potential of supporting walls.[31–34] For such a case an additional pressure field is created, which in turn leads to an enhanced hydrodynamic dispersion that is often beneficial for the mixing process.

The works indicated above have considered the solute dispersion under a steady DC electric field. However, there are several advantages of EOF under an AC electric field. Gas bubbles are often very detrimental in microchannels, since they may block the flow passage. It is noteworthy to mention that an AC electric based EOF has one major advantage over DC EOF: under DC field gas bubbles are produced at the electrodes driving the flow, while bubble formation is suppressed under AC fields. Besides, the AC electric field based EOF requires lower voltage drop compared to the DC EOF, which reduces the chances of damage of electrodes, requires a less response time leading to a faster detection time as well as minimizes the electrode erosion, to name a few.[35–37] Note that the AC electric field based EOF is further desirable for many practical applications, e.g., electrokinetic manipulation of nanoparticulates, rapid medical diagnosis, etc.[38,39] There are several studies dealing with electrohydrodynamics through microdevices under an AC electric field,[40–47] however little attention is paid to study the solute dispersion under AC electric field based EOF. Huang and Lai studied the impact of AC electric field based EOF on the transport and separation phenomena through a two dimensional microchannel.[48] Ramon et al. studied the dispersion of solutes under an oscillatory EOF across a cylindrical tube considering the reversible mass exchange along the walls and it is observed that the separation of species can be done in a better way under an AC electric field.[49] The solute dispersion through a microchannel considering the combined impact of time dependent electric field as well as wall ζ-potential was studied by Paul and Ng.[50] Teodoro et al. have investigated the impact of oscillatory EOF on the solute dispersion under various periodic electric fields (e.g., sawtooth, square, and parabolic waveforms, etc.) and they observed that an enhanced mass transport can be achieved suitably regulating the field signal.[51] Li and Jian studied solute dispersion under an AC electric field driven EOF and deduced the results for the dispersion coefficient and the mean concentration of the solutes across a microtube.[52]

The aforesaid articles deal with the solute dispersion in fluidic devices with bare walls (or rigid walls) and a single phase

fluidic medium under an AC electric field driven oscillatory EOF. Kumar and De studied the hydrodynamic dispersion of solutes under an oscillatory EOF across microtubes with porous walls.[53] Li and Jian studied the impact of an AC field induced EOF on the solute dispersion across a soft nanochannel.[54] Reshadi and Saidi studied the solute dispersion through a soft nanochannel under steady as well as oscillatory electroosmotic-Poiseuille flow.[55] Note that the soft nanochannels are conduits in which the inner side of the supporting rigid walls are coated with a soft polyelectrolyte layer. It is shown in the existing studies that the presence of polyelectrolyte layers can have a substantial impact on the dispersion process.[56,57] Note that solute dispersion driven by an oscillatory electric field finds potential application in various fields, including biological or physiological transport, drug delivery systems, and chromatographic separation and mixing, to name a few.[58–62]

In recent years, a significant work is done on the flow modulation and transport of ionic species through various shaped engineered soft nanochannels. Karimzadeh *et al.* studied the impact of the shape of soft nanochannels on the overall EOF modulation and transport of ionic species.[63] Dartoomi *et al.* have shown the importance of the shape of nanochannels on the blue energy generation.[64] Such an extensive study indicates an alternate way to extract the energy. Ashrafizadeh and co-researchers studied extensively the role of nanochannel geometry and soft layers in the salinity gradient driven energy harvesting through various shaped soft nanochannels.[65–67] In addition to the flow modulation through a soft nanochannel, another important electrokinetic phenomenon is ionic current rectification (ICR). Note that the ICR is a consequence of symmetry breaking either in channel geometry, charge distribution, the applied potential gradient, *etc.*[68] For such cases, depending on the voltage bias the ion transport is preferential along a particular direction. In recent years, several researchers studied extensively the ICR phenomenon though various engineered microdevices for which there is some underlying asymmetry.[69–72] It is noteworthy to mention that in the absence of any asymmetry along the lateral dimension, the no current rectification is possible.[73]

In addition to soft nanochannels, a huge body of literature is further available on the modulation of electrokinetic flow through microfluidic devices filled with two or more liquids. The existing studies in this direction are carried out under DC or AC electric fields and are restricted only with the study on electrohydrodynamics.[74–81] In the present article, we focus on dispersion of passive solutes under an AC electric field driven EOF across a channel filled with an electrolyte solution surrounded with a layer of a membrane of various biological cells. Such a membrane layer may bear additional mobile charges (*e.g.*, free lipid molecules, charged surfactant molecules in the form of dimer micelles or small micelles with very low aggregation numbers). The presence of free charges across the membrane layer gives rise to non zero charge density along the liquid–liquid interface.[82,83] According to the fluid mosaic model of Singer and Nicolson,[84] the membrane layer can be treated as a two-dimensional oriented viscous liquid with low

dielectric constant. The difference in dielectric permittivity of the aqueous electrolyte solution and the membrane layer leads to the ion partitioning effect.[85,86] Depending on the Born energies of both the phases with possible mismatch in dielectric permittivity, the electrolyte ions will penetrate inside the peripheral membrane layer in a discontinuous manner. It is noteworthy to mention that in a recent article we have studied the solute dispersion through a soft nanochannel under the EOF induced by the applied DC electric field.[57] In contrast, the present article deals with the flow modulation and the solute dispersion under applied AC electric field. Furthermore, instead of a soft nanochannel we consider the EOF modulation and solute dispersion in a nanochannel filled with electrolyte solution surrounded by a layer of a dielectric liquid that resembles membranes of various biological cells. Note that there is no available study in this direction that deals with the flow modulation under an oscillatory electric field and the impact of modulated EOF on the dispersion of solutes across such a channel.

In order to fill the aforesaid research gap, we aim to study the flow modulation and solute dispersion across such a channel indicated above under applied AC electric field. A mathematical study is thus performed to evaluate the EOF field and its impact on solute dispersion considering the combined impact of the ion partitioning and the ion steric effects. Note that a steric effect is induced by the interaction of finite sized ions. We adopt the Carnahan and Starling model to take into account the ion steric effect,[87] which is however best suited to characterize the said effect for a moderate to highly charged electrohydrodynamic systems.[88,89] Considering the impact of molecular diffusion and modulated AC field based EOF, the band broadening process is analysed by the generalized dispersion model introduced by Gill and Sankarasubramanian.[9] Note that the AC electric field driven EOF prevents the formation of gas bubbles within the flow passage, and thus the fluid convection is expected to have a substantial impact on the solute dispersion process.

The rest of the article is organized as follows. The problem formulation is summarized in Section 2. The mathematical model and methodology are presented in Section 3, which includes a brief description of the distribution of electrostatic EDL potential, AC electric field driven oscillatory EOF and the solute dispersion process. We developed a numerical scheme to simulate the governing equations. In addition, we obtained closed forms of analytical results that describe the EOF field as well as the dispersion process under various limiting cases. Results and discussion on the modulation of EOF and its impact on the solute dispersion process are included in Section 4 followed by a brief summary of all the results and future scope of study in Section 5.

2 Problem formulation

Fig. 1 systematically depicts a parallel plate slit nanochannel of height $2H$ filled with an electrolyte solution surrounded by a
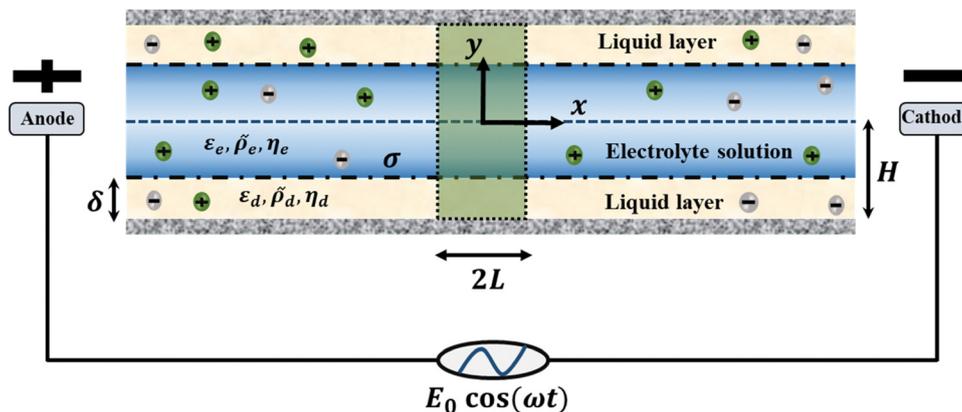
Fig. 1 Schematic representation of the EOF through an infinitely long nanochannel filled with an electrolyte solution surrounded by a layer of a dielectric liquid. The dielectric permittivity, fluidic mass density and viscosity of the liquid layer and ambient electrolyte solutions are denoted as ϵ_d, $\tilde{\rho}_d$, η_d and ϵ_e, $\tilde{\rho}_e$, η_e, respectively. The uncharged solute with concentration C_0 is placed initially along the middle of the channel with bandwidth $2L$, which is further exposed to a back and forth fluid motion under an oscillating electric field $E_0 \cos(\omega t)$.

layer of an immiscible and dielectric liquid with thickness δ ($<H$). We neglect the end effects considering the width and length of the channel are much larger than its height. A Cartesian coordinate system (x, y) with the origin located at the channel center is employed to analyze the EOF field and solute dispersion under the influence of an AC electric field $\mathbf{E}(t) = (\Re\{E_0 \exp(-i\omega t)\}, 0, 0)$, where E_0 indicates the magnitude of applied oscillatory electric field. Here $i = \sqrt{-1}$; ω and t indicate the angular frequency of the oscillatory electric field and time, respectively, and $\Re\{\mathcal{Z}\}$ indicates the real part of a complex number $\mathcal{Z}$. The concentration and valence of additional mobile ions in the form of surfactant molecules present in the membrane layer are denoted as N_0 (in mM) and Z, respectively. We have assumed that the concentration of such molecules with in an aqueous medium is zero.

This is a reasonable assumption as their solubility in the aqueous phase is negligibly small.[82,90] The presence of the additional mobile charges within the dielectric liquid layer induces nonzero interfacial charge σ, which further leads to the formation of two EDLs along the liquid–liquid interface. Such EDLs may form due to attraction of counterions by the charged liquid–liquid interface from the adjacent liquid medium. An EDL may form at the interface towards the side of aqueous medium with thickness κ^{-1}, while an equivalent EDL with thickness κ_d^{-1} further forms at the liquid–liquid interface towards the dielectric liquid layer side. A detailed description of the same may be found elsewhere.[82,86] We consider the background electrolyte as a binary symmetric $z{:}z$ electrolyte with bulk concentration n_0 (in mM). The viscosity and dielectric permittivity of the membrane layer are denoted as η_d, η_e and ϵ_d, ϵ_e, respectively. The dielectric constant of the membrane layer is in general lower than that of the electrolyte medium.[83,91] Thus, the penetration of electrolyte ions within the membrane layer occurs in a discontinuous manner due to the presence of the ion partitioning effect. The concentration of electrolyte ions ($n_j, j = 1, 2$) along the liquid–liquid interface is discontinuous and satisfies the following relation[92–95]

$$n_j\{(-H + \delta)^-\} = f_j n_j\{(-H + \delta)^+\}, \quad j = 1, 2 \qquad (1)$$

where f_j indicates the ion partitioning coefficient of the jth ($j = 1, 2$) ions and is defined as ref. 96

$$f_{j(j=1,2)} = \exp\left\{ -\left(\frac{1}{k_B T} \right) \frac{(ze)^2}{8\pi r_j} \left(\frac{1}{\epsilon_d} - \frac{1}{\epsilon_e} \right) \right\} \qquad (2)$$

Here k_B, T and e are the Boltzmann constant, the absolute temperature and the elementary charge, respectively, and the radius of the jth ion is denoted as r_j ($j = 1, 2$). In our present study, we consider the size of the cation and anion to be the same denoted as r, and thus $f_1 = f_2 = f$. It is evident from the relation (2) that for a two-phase fluidic system with different dielectric permittivities of liquids in the adjacent phases, an increase in the ion size increases the value of ion partitioning coefficient f. Thus, an increase in the ion size reduces the dielectric-gradient mediated ion partitioning effect. Thus, both the ion steric and ion partitioning effects are coupled together. However, for similar dielectric permittivity of the adjacent phases, the ion partitioning effect is absent.

Using the Carnahan and Starling model,[87] the spatial distribution of the concentration of mobile electrolyte ions ($n_j, j = 1, 2$) with finite size follows the modified Boltzmann distribution, given as[97]

$$n_j(y) = \frac{n_0 \exp\left(-\dfrac{z_j F \psi}{RT} \right)}{1 + P\left\{ \cosh\left(\dfrac{zF\psi}{RT} \right) - 1 \right\}}, \quad j = 1, 2 \qquad (3)$$

The terms ψ, F and R indicate the electrostatic potential, Faraday constant and gas constant, respectively. The above expression further involves the steric factor P, defined as $P = 8\phi_B/(1 + 8\phi_B)$, where ϕ_B is the volume fraction of mobile ions, defined as $\phi_B = (4\pi r^3/3)2N_A n_0$. Here N_A is the Avogadro number. In addition, the spatial distribution of the concentration of additional mobile ions present in the dielectric liquid layer, considering its nonzero volume fraction ϕ_d, is given as

follows[83,97]

$$n_d(y) = N_0 \frac{\exp\left\{-\frac{ZF}{RT}(\psi - \psi_D)\right\}}{(1 - \Omega) + \Omega \exp\left\{-\frac{ZF}{RT}(\psi - \psi_D)\right\}} \quad (4)$$

where $\Omega = 8\phi_d/(1 + 8\phi_d)$. The volume fraction ϕ_d is defined as $\phi_d = (4\pi a_d^3/3)2N_A N_0$, where a_d indicates the size of the additional ion. The expression (4) involves the Donnan potential ψ_D which indicates the potential deep inside the dielectric liquid layer.[83-98] Explicit expression for the same is deduced later. The readers are further referred to the Section S.1 (ESI†) for a detailed derivation of relation (4).

The EOF field across the considered channel is in general lies in the creeping flow regime and there is no instability occurring in the present two-liquid systems. As indicated earlier the liquid in the dielectric liquid layer and the aqueous medium are immiscible in nature, so the liquid in the layer adjacent to the supporting walls and the aqueous medium cannot permeate each other. Furthermore, we assume that the uniformly charged liquid–liquid interface remains planar, which is in fact the basic state of a general stability problem. Note that for the considered parameter space, the Capillary number is far smaller than unity, and accordingly, warrants our analysis without accounting the deformation of the liquid–liquid interface. Such a consideration is rather common in transient EOF involving liquid–liquid interface.[74-78,80,81] A small amount of passive solute is placed along the channel center with a given bandwidth, and it faces the back and forth EOF induced by an applied AC electric field. The flow background liquid medium is not affected by the presence of a dilute band of sufficiently small soluble solutes. The details of the mathematical model and methods to solve the set of model equations are described below.

3 Mathematical model and methodology

In this section, we present the detailed mathematical model and methodology to solve the set of governing equations. For the considered flow geometry, the EDL potential, flow field and spatial distribution of the concentration are symmetric with respect to the central line of the channel. Without loss of generality we present the governing equations pertaining to the EDL potential, EOF field as well as concentration distribution of solutes along the lower half of the channel. We first present the electrostatic EDL potential followed by the calculation of AC electric field based EOF. With the known flow field, the dispersion characteristics of the injected solute under oscillatory EOF field are further analyzed.

3.1 Electrostatic EDL potential and EOF field under AC electric field

The electrostatic EDL potential considering the combined impact of the ion steric and the ion partitioning effects is described by the modified Poisson–Boltzmann equation, given as

$$-\epsilon_d \frac{d^2\psi}{dy^2} = \rho_d(y): \quad -H < y \leq -H + \delta \quad (5a)$$

$$-\epsilon_e \frac{d^2\psi}{dy^2} = \rho_e(y): \quad -H + \delta < y \leq 0 \quad (5b)$$

where $\rho_d(y)$ and $\rho_e(y)$ represent the volumetric charges due to mobile ions inside and outside of the dielectric liquid layer, respectively, and are defined as

$$\rho_d(y) = F[f\{zn_1(y) - zn_2(y)\} + Zn_d(y)] \quad -H < y \leq -H + \delta \quad (6a)$$

$$\rho_e(y) = F[zn_1(y) - zn_2(y)] \quad -H + \delta < y \leq 0 \quad (6b)$$

Substituting the relations (3) and (6) into the eqn (5) yields

$$\frac{d^2\psi}{dy^2} = \frac{2Fn_0zf}{\epsilon_d}\left[\frac{\sinh\left(\frac{zF\psi}{RT}\right)}{1 + P\left\{\cosh\left(\frac{zF\psi}{RT}\right) - 1\right\}}\right.$$
$$\left. - \frac{ZN_0}{2fn_0z}\left(\frac{\exp\left\{-Z\left(\frac{F\psi}{RT} - \frac{F\psi_D}{RT}\right)\right\}}{(1 - \Omega) + \Omega\exp\left\{-Z\left(\frac{F\psi}{RT} - \frac{F\psi_D}{RT}\right)\right\}}\right)\right]$$
$$-H < y \leq -H + \delta \quad (7a)$$

$$\frac{d^2\psi}{dy^2} = \frac{2Fn_0z}{\epsilon_e}\left[\frac{\sinh\left(\frac{zF\psi}{RT}\right)}{1 + P\left\{\cosh\left(\frac{zF\psi}{RT}\right) - 1\right\}}\right] \quad (7b)$$
$$-H + \delta < y \leq 0.$$

The channel walls are considered to be uncharged. We adopt the continuity of electrostatic EDL potential along the liquid–liquid interface. In the presence of interfacial charge, the displacement vector along the liquid–liquid interface is discontinuous. Along the central line, the gradient of potential vanishes due to symmetry. We use the scale $\phi_0 = RT/zF$ to non-dimensionalize the EDL potential ($\psi(y)$) as well as the Donnan potential (ψ_D) and the space coordinate y is scaled by the half height of the channel, $i.e.$, H. Using the above scales the governing equation and associated boundary conditions for the EDL potential in the scaled form may be deduced as follows

$$\frac{d^2\bar{\psi}}{d\bar{y}^2} = (\kappa_1 H)^2\left[\frac{\sinh(\bar{\psi})}{1 + P\{\cosh(\bar{\psi}) - 1\}}\right.$$
$$\left. - M\left(\frac{\exp\left\{-\frac{Z}{z}(\bar{\psi} - \bar{\psi}_D)\right\}}{(1 - \Omega) + \Omega\exp\left\{-\frac{Z}{z}(\bar{\psi} - \bar{\psi}_D)\right\}}\right)\right] \quad (8a)$$
$$-1 < \bar{y} \leq -1 + \bar{\delta}$$

$$\frac{d^2\bar{\psi}}{d\bar{y}^2} = (\kappa H)^2 \left[\frac{\sinh(\bar{\psi})}{1 + P\{\cosh(\bar{\psi}) - 1\}}\right] \quad -1 + \bar{\delta} < \bar{y} \le 0. \quad (8b)$$

subject to the boundary conditions

$$\frac{d\bar{\psi}}{d\bar{y}}\bigg|_{\bar{y}=-1} = 0 \quad (9a)$$

$$\bar{\psi}(\bar{y})\big|_{\bar{y}=(-1+\bar{\delta})^-} = \bar{\psi}(\bar{y})\big|_{\bar{y}=(-1+\bar{\delta})^+} \quad (9b)$$

$$\epsilon_R \frac{d\bar{\psi}}{d\bar{y}}\bigg|_{\bar{y}=(-1+\bar{\delta})^-} - \frac{d\bar{\psi}}{d\bar{y}}\bigg|_{\bar{y}=(-1+\bar{\delta})^+} = \bar{\sigma} \quad (9c)$$

$$\frac{d\bar{\psi}}{d\bar{y}}\bigg|_{\bar{y}=0} = 0. \quad (9d)$$

Eqn (8a) involves the scaled parameter M, defined as $M = ZN_0/2zfn_0$. The quantities $\bar{\psi}(\bar{y})$, $\bar{\psi}_D$ indicate the scaled EDL potential and Donnan potential, respectively. The scaled interfacial charge $\bar{\sigma}$ is defined as $\bar{\sigma} = \sigma H/\epsilon_e\phi_0$ and $\epsilon_R = \epsilon_d/\epsilon_e$ indicates the liquid layer to electrolyte permittivity ratio with $\bar{\delta} = \delta/H$ being the scaled thickness of the liquid layer. The quantity κ appearing in eqn (8) indicates the inverse of the EDL thickness (which forms towards the side of the aqueous phase), defined as $\kappa = \sqrt{2F^2z^2n_0/\epsilon_e RT}$ and the quantity κ_1 appearing in eqn (8) is defined as $\kappa_1 = \kappa\sqrt{f\epsilon_e/\epsilon_d}$. The scaled Donnan potential can be obtained by setting the right hand side of eqn (8a) to zero, and thus we may write

$$\frac{\sinh(\bar{\psi}_D)}{1 + P\{\cosh(\bar{\psi}_D) - 1\}} = M \quad (10)$$

Solution of (10) provides the explicit expression for the scaled Donnan potential, given as

$$\bar{\psi}_D = \ln\left\{\frac{M(1-P) + \sqrt{M^2 - 2M^2P + 1}}{1 - MP}\right\} \quad (11)$$

The time dependent axial flow velocity component $u(y, t)$ is governed by the unsteady Stokes equations with the electric body force term, and is given as

$$\eta_d \frac{\partial^2 u(y,t)}{\partial y^2} + \rho_d(y)E(t) = \tilde{\rho}_d \frac{\partial u(y,t)}{\partial t} \\ -H < y \le -H + \delta \quad (12a)$$

$$\eta_e \frac{\partial^2 u(y,t)}{\partial y^2} + \rho_e(y)E(t) = \tilde{\rho}_e \frac{\partial u(y,t)}{\partial t} \quad -H + \delta < y \le 0 \quad (12b)$$

subject to the boundary conditions

$$u(y, t)\big|_{y=-H} = 0 \quad (13a)$$

$$u(y, t)\big|_{y=(-H+\delta)^-} = u(y, t)\big|_{y=(-H+\delta)^+} \quad (13b)$$

$$\eta_d \frac{du(y,t)}{dy}\bigg|_{y=(-H+\delta)^-} - \eta_e \frac{du(y,t)}{dy}\bigg|_{y=(-H+\delta)^+} = \sigma E(t) \quad (13c)$$

$$\frac{du(y,t)}{dy}\bigg|_{y=0} = 0. \quad (13d)$$

where the mass density of the liquid in the peripheral layer and electrolyte solution are $\tilde{\rho}_d$ and $\tilde{\rho}_e$, respectively. We consider the no-slip velocity boundary condition along the supporting rigid walls of the channel as indicated in the relation (13a). The continuity of flow velocity along the liquid–liquid interface is adopted, which is further indicated in the relation (13b). We adopt the EDL plus surface charge (SC) model to study the considered electrokinetic flow involving a two-liquid system.[74] It is noteworthy to mention that such an EDL plus SC model can successfully describe the experimental observation on the electrokinetic behavior of two-phase liquid systems.[99] Such a consideration may leads to the condition indicated in (13c). We further adopt symmetry condition for flow velocity along the central line of the channel, which is indicated in (13d).

We consider the oscillatory EOF under AC electric field $\mathbf{E}(t) = (\Re\{E_0 \exp(-i\omega t)\}, 0, 0)$ and thus the back and forth oscillatory axial velocity may be written as $u(y, t) = \Re\{u_0(y) \exp(-i\omega t)\}$, where $u_0(y)$ is the complex amplitude of the velocity field. We consider the Helmoltz–Smoluchowsky reference velocity $U_{HS} = \epsilon_e\phi_0 E_0/\eta_e$ as the velocity scale. Below we recast the governing equations and boundary conditions associated with the velocity field in the scaled form

$$\frac{d^2\bar{u}_0}{d\bar{y}^2} - \frac{\epsilon_R}{\eta_R}\frac{d^2\bar{\psi}}{d\bar{y}^2} = -\frac{i\omega\tilde{\rho}_d H^2}{\eta_d}\bar{u}_0 \quad -1 < y \le -1 + \bar{\delta} \quad (14a)$$

$$\frac{d^2\bar{u}_0}{d\bar{y}^2} - \frac{d^2\bar{\psi}}{d\bar{y}^2} = -\frac{i\omega\tilde{\rho}_e H^2}{\eta_e}\bar{u}_0 \quad -1 + \bar{\delta} < \bar{y} \le 0 \quad (14b)$$

subject to

$$\bar{u}_0(\bar{y})\big|_{\bar{y}=-1} = 0 \quad (15a)$$

$$\bar{u}_0(\bar{y})\big|_{\bar{y}=(-1+\bar{\delta})^-} = \bar{u}_0(\bar{y})\big|_{\bar{y}=(-1+\bar{\delta})^+} \quad (15b)$$

$$\eta_R \frac{d\bar{u}_0}{d\bar{y}}\bigg|_{\bar{y}=(-1+\bar{\delta})^-} - \frac{d\bar{u}_0}{d\bar{y}}\bigg|_{\bar{y}=(-1+\bar{\delta})^+} = \bar{\sigma} \quad (15c)$$

$$\frac{d\bar{u}_0}{d\bar{y}}\bigg|_{\bar{y}=0} = 0. \quad (15d)$$

where $\bar{u}_0(\bar{y})$ is the scaled value $u_0(y)$ and $\eta_R = \eta_d/\eta_e$ is the viscosity ratio. Solving the above eqn (14a) and (14b) subject to the given boundary conditions (15a)–(15d) yields the explicit form of $\bar{u}_0(\bar{y})$, given as

$$\bar{u}_0(\bar{y}) = \begin{cases} C_1\cosh(m_1\bar{y}) + C_2\sinh(m_1\bar{y}) + \frac{(m_1 m_2)^2}{2m_1}[\exp(m_1\bar{y})J_1(\bar{y}) - \exp(-m_1\bar{y})J_2(\bar{y})] + m_2^2\bar{\psi}(\bar{y}); & -1 < \bar{y} \le -1 + \bar{\delta} \\ \\ C_3\cosh(m_3\bar{y}) + C_4\sinh(m_3\bar{y}) + \frac{m_3}{2}[\exp(m_3\bar{y})J_3(\bar{y}) - \exp(-m_3\bar{y})J_4(\bar{y})] + \bar{\psi}(\bar{y}); & -1 + \bar{\delta} < \bar{y} \le 0 \end{cases} \quad (16)$$

The above expression (16) contains several constants, *e.g.*, m_i ($i = 1, 2, 3$) and C_i ($i = 1, 2, 3, 4$) and integrals $J_i(\bar{y})$ ($i = 1, 2, 3, 4$), which are are provided in Appendix-A.

It is evident that one can deduce the results for the axial velocity field with the known value of the electrostatic EDL potential. In Appendix-B, we have deduced the approximate semi-analytical results for EDL potential valid for the low to higher regime of electrostatic charge. In addition, we have further deduced exact analytical results for electrostatic potential as well as velocity field within the Debye–Hückel electrostatic limit and are summarized in Appendix-C. However to consider a broad range of electrostatic charge as well as other model parameters, we have deduced numerical results for EDL potential using the finite difference based numerical scheme. The discretized equation for EDL potential based on the central difference scheme is solved iteratively using the tridiagonal matrix algorithm. The iterations are continued until the difference in two successive steps becomes smaller than the tolerance limit. A comparison of the numerical results for EDL potential with the deduced semi-analytical results are shown in Appendix-B and the exact theoretical results under the Debye–Hückel limit are shown in Appendix-C. With the known value of EDL potential and the integrals mentioned above, we have further deduced the numerical results of axial velocity using the expression (16). Note that the main complexity to deduce the axial velocity is to calculate the integrals J_i ($i = 1, 2, 3, 4$) and for the same we have used MATHEMATICA software. The validation of dynamic axial velocity field with the deduced analytical results is provided in Appendix-C. The results for the velocity field are further used to study the dispersion characteristics of the solute band placed inside the channel. A detailed description of the dispersion process is summarized below.

3.2 Dispersion of solutes

In this subsection we have presented the governing equation for the concentration of solutes and the relevant initial and boundary conditions to study the dispersion process. A solute with bandwidth $2L$, diffusivity D_0 and initial concentration C_0 is placed at the channel center and is exposed under oscillatory EOF. The concentration distribution of the solutes is governed by the unsteady convective–diffusion equation, given as

$$\frac{\partial C}{\partial t} + u(y, t)\frac{\partial C}{\partial x} = D_0\left(\frac{\partial^2 C}{\partial x^2} + \frac{\partial^2 C}{\partial y^2}\right) \tag{17}$$

where $C(x, y, t)$ indicates the concentration of solutes. The initial distribution of the concentration of solutes is given as

$$C(x, y, 0) = \begin{cases} C_0, & \text{when } |x| \leq L \\ 0, & \text{when } |x| > L \end{cases} \tag{18}$$

Along $x \to \pm\infty$, the concentration of the solute vanishes. Besides, there is no mass transfer across the supporting rigid walls. We further adopt the symmetry condition along the central line of the channel. Thus, the boundary conditions associated with the solute concentration are as follows

$$C(\pm\infty, y, t) = 0 \tag{19a}$$

$$\frac{\partial C(x, -H, t)}{\partial y} = 0 = \frac{\partial C(x, 0, t)}{\partial y} \tag{19b}$$

The reference concentration C_0 is considered as the scale for the solute concentration. The y-coordinate is scaled by the half-height of the channel, *i.e.*, H. Besides, the x-coordinate is scaled by $H^2 U_{\text{HS}}/D_0$ and the time is scaled by H^2/D_0. Using these scales, we may obtain the governing equation and associated initial and boundary conditions in the nondimensional form, given as

$$\frac{\partial \bar{C}}{\partial \bar{t}} + \bar{u}(\bar{y}, \bar{t})\frac{\partial \bar{C}}{\partial \bar{x}} = \frac{\partial^2 \bar{C}}{\partial \bar{y}^2} + \frac{1}{\text{Pe}^2}\frac{\partial^2 \bar{C}}{\partial \bar{x}^2} \tag{20}$$

subject to the initial conditions

$$\bar{C}(\bar{x}, \bar{y}, 0) = \begin{cases} 1, & \text{when } |\bar{x}| \leq \bar{L} \\ 0, & \text{when } |\bar{x}| > \bar{L} \end{cases} \tag{21}$$

and boundary conditions

$$\bar{C}(\pm\infty, \bar{y}, \bar{t}) = 0 \tag{22a}$$

$$\frac{\partial \bar{C}(\bar{x}, -1, \bar{t})}{\partial \bar{y}} = 0 = \frac{\partial \bar{C}(\bar{x}, 0, \bar{t})}{\partial \bar{y}}. \tag{22b}$$

where $\bar{C} = C/C_0$, $\bar{x} = D_0 x/H^2 U_{\text{HS}}$, $\bar{t} = D_0 t/H^2$ and $\bar{L} = D_0 L/H^2 U_{\text{HS}}$. The non-dimensional parameter Pe indicates the ratio of the rate of transport caused by convection and molecular diffusion, and is defined as Pe $= H U_{\text{HS}}/D_0$. To analyze the dispersion of solutes we introduce a moving coordinate system, comoving with the cross-sectional mean fluid velocity $\bar{u}_{\text{m}}(\bar{t}) = \int_{-1}^{0}\bar{u}(\bar{y}, \bar{t})\mathrm{d}\bar{y}$. Thus, the new axial coordinate $\bar{x}_{\text{u}}(\bar{x}, \bar{t})$ (in the scaled form) in the moving frame of reference may be defined as

$$\bar{x}_{\text{u}}(\bar{x}, \bar{t}) = \bar{x} - \int_0^{\bar{t}}\bar{u}_{\text{m}}(\tau)\mathrm{d}\tau, \tag{23}$$

Using this transformation, we may recast the unsteady convection–diffusion equation as follows

$$\frac{\partial \bar{C}}{\partial \bar{t}} + (\bar{u}(\bar{y}, \bar{t}) - \bar{u}_{\text{m}}(\bar{t}))\frac{\partial \bar{C}}{\partial \bar{x}_{\text{u}}} = \frac{\partial^2 \bar{C}}{\partial \bar{y}^2} + \frac{1}{\text{Pe}^2}\frac{\partial^2 \bar{C}}{\partial \bar{x}_{\text{u}}^2} \tag{24}$$

The method used by Gill and Sankarasubramanian[9] is adopted to study the dispersion process. Thus, the local concentration of solutes can be written in terms of series expansion in axis gradients of cross-sectional averaged concentration $\bar{C}_{\text{m}}$, given as

$$\bar{C}_{\text{m}} = \bar{C}_{\text{m}} + \sum_{k=1}^{\infty} f_k(\bar{y}, \bar{t})\frac{\partial^k \bar{C}}{\partial \bar{x}_{\text{u}}^k} \tag{25}$$

where

$$\bar{C}_{\text{m}}(\bar{x}_u, \bar{t}) = \int_{-1}^{0}\bar{C}(\bar{x}_{\text{u}}, \bar{y}, \bar{t})\mathrm{d}\bar{y} \tag{26}$$

The terms $f_k(\bar{y}, \bar{t})$ ($k = 1, 2, 3, \ldots$) are the coefficients of series expansion. Substituting (26) into (25) yields

$$\begin{aligned}\frac{\partial \bar{C}_{\text{m}}}{\partial \bar{t}} + (\bar{u} - \bar{u}_{\text{m}})\frac{\partial \bar{C}_{\text{m}}}{\partial \bar{x}_{\text{u}}} &= \frac{1}{\text{Pe}^2}\frac{\partial^2 \bar{C}_{\text{m}}}{\partial \bar{x}_{\text{u}}^2} - \sum_{k=1}^{\infty}\left\{\left(\frac{\partial f_k}{\partial \bar{t}} - \frac{\partial^2 f_k}{\partial \bar{y}^2}\right)\frac{\partial^k \bar{C}_{\text{m}}}{\partial \bar{x}_{\text{u}}^k}\right.\\ &\quad + f_k(\bar{u} - \bar{u}_{\text{m}})\frac{\partial^{k+1}\bar{C}_{\text{m}}}{\partial \bar{x}_{\text{u}}^{k+1}}\\ &\quad \left. + f_k\frac{\partial^{k+1}\bar{C}_{\text{m}}}{\partial \bar{t}\partial \bar{x}_{\text{u}}^k} - \frac{f_k}{\text{Pe}^2}\frac{\partial^{k+2}\bar{C}_{\text{m}}}{\partial \bar{x}_{\text{u}}^{k+2}}\right\}\end{aligned}$$

$$\tag{27}$$

We consider that the dispersion process is diffusive right from the time zero and thus the cross-sectional averaged concentration $\bar{C}_m$ follows the given equation[100]

$$\frac{\partial \bar{C}_m}{\partial \bar{t}} = \sum_{i=1}^{\infty} K_i(\bar{t}) \frac{\partial^i \bar{C}_m}{\partial \bar{x}_u^i} \tag{28}$$

where the coefficients $K_i(\bar{t})$ are the periodic function of time due to an oscillatory flow of the background aqueous medium. Considering k-times the partial derivative of the above eqn (28) with respect to space coordinate $\bar{x}_u$, we may deduce the following relation

$$\frac{\partial^{k+1} \bar{C}_m}{\partial \bar{t} \partial \bar{x}_u^k} = \sum_{i=1}^{\infty} K_i(\bar{t}) \frac{\partial^{k+i} \bar{C}_m}{\partial \bar{x}_u^{k+i}} \tag{29}$$

Now substituting eqn (28) and (29) into eqn (27) and after algebraic simplification yields

$$\left\{\frac{\partial f_1}{\partial \bar{t}} - \frac{\partial^2 f_1}{\partial \bar{y}^2} + (\bar{u}(\bar{y}, \bar{t}) - \bar{u}_m(\bar{t}) + K_1(\bar{t}))\right\} \frac{\partial \bar{C}_m}{\partial \bar{x}_u}$$

$$+ \left\{\frac{\partial f_2}{\partial \bar{t}} - \frac{\partial^2 f_2}{\partial \bar{y}^2} + (\bar{u}(\bar{y}, \bar{t}) - \bar{u}_m(\bar{t}) + K_1(\bar{t})) f_1\right.$$

$$+ \left.\left(K_2(\bar{t}) - \frac{1}{\mathrm{Pe}^2}\right)\right\} \frac{\partial^2 \bar{C}_m}{\partial \bar{x}_u^2} + \left\{\frac{\partial f_{k+2}}{\partial \bar{t}} - \frac{\partial^2 f_{k+2}}{\partial \bar{y}^2} + (\bar{u}(\bar{y}, \bar{t}) - \bar{u}_m(\bar{t}) + K_1(\bar{t})) f_{k+1}\right.$$

$$+ \left.\left(K_2(\bar{t}) - \frac{1}{\mathrm{Pe}^2}\right) f_k + \sum_{i=3}^{k+2} K_i(\bar{t}) f_{k+2-i}\right\} \frac{\partial^{k+2} \bar{C}_m}{\partial \bar{x}_u^{k+2}} = 0, \quad (k = 1, 2, 3, \ldots) \tag{30}$$

From the above equation we may set the coefficients of $\partial^k \bar{C}_m / \partial \bar{x}_u^k$ (k = 1, 2, 3, …) to zero, which yields the following differential equations involving f_k

$$\frac{\partial f_1}{\partial \bar{t}} - \frac{\partial^2 f_1}{\partial \bar{y}^2} + (\bar{u}(\bar{y}, \bar{t}) - \bar{u}_m(\bar{t}) + K_1(\bar{t})) = 0 \tag{31a}$$

$$\frac{\partial f_2}{\partial \bar{t}} - \frac{\partial^2 f_2}{\partial \bar{y}^2} + (\bar{u}(\bar{y}, \bar{t}) - \bar{u}_m(\bar{t}) + K_1(\bar{t})) f_1 + \left(K_2(\bar{t}) - \frac{1}{\mathrm{Pe}^2}\right) = 0 \tag{31b}$$

$$\frac{\partial f_{k+2}}{\partial \bar{t}} - \frac{\partial^2 f_{k+2}}{\partial \bar{y}^2} + (\bar{u}(\bar{y}, \bar{t}) - \bar{u}_m(\bar{t}) + K_1(\bar{t})) f_{k+1}$$

$$+ \left(K_2(\bar{t}) - \frac{1}{\mathrm{Pe}^2}\right) f_k + \sum_{i=3}^{k+2} K_i(\bar{t}) f_{k+2-i} = 0 \tag{31c}$$

The index k in eqn (31c) takes the values k = 1, 2, 3, …. It is worth noting that the initial and boundary conditions for $\bar{C}$ are also satisfied by $\bar{C}_m$. Thus, substituting (25) into (21) and (22) yields

$$f_k(\bar{y}, 0) = 0 \tag{32}$$

and

$$\left.\frac{\partial f_k(\bar{y}, \bar{t})}{\partial \bar{y}}\right|_{\bar{y}=-1} = \left.\frac{\partial f_k(\bar{y}, \bar{t})}{\partial \bar{y}}\right|_{\bar{y}=0} = 0 \tag{33}$$

Besides, eqn (26) requires

$$\int_{-1}^{0} f_k(\bar{y}, \bar{t}) \mathrm{d}\bar{y} = 0 \tag{34}$$

Integrating (31a)–(31c) with respect to $\bar{y}$ from -1 to 0, one can easily check that the coefficient $K_1(\bar{t})$ vanishes and the other coefficients are derived as follows

$$K_2(\bar{t}) = \frac{1}{\mathrm{Pe}^2} - \int_{-1}^{0} (\bar{u}(\bar{y}, \bar{t}) - \bar{u}_m(\bar{t})) f_1(\bar{y}, \bar{t}) \mathrm{d}\bar{y} \tag{35}$$

and

$$K_{k+2}(\bar{t}) = -\int_{-1}^{0} (\bar{u}(\bar{y}, \bar{t}) - \bar{u}_m(\bar{t})) f_{k+1}(\bar{y}, \bar{t}) \mathrm{d}\bar{y}, \quad k = 1, 2, 3, \ldots \tag{36}$$

Note that the term $K_1(\bar{t})$ indicates the convection coefficient due to the velocity of solutes and thus vanishes as we are in a moving frame of reference. Besides, the term $K_2(\bar{t})$ indicates the effective dispersion coefficient due to the molecular diffusion and fluid convection, which is renamed as $K(\bar{t})$. The terms K_i ($i \geq 3$) are very small compared to the value of K_2. So, we can neglect the contribution of all K_i when $i \geq 3$.[9] Thus, eqn (28) takes the simplified form as follows

$$\frac{\partial \bar{C}_m}{\partial \bar{t}} = K_2(\bar{t}) \frac{\partial^2 \bar{C}_m}{\partial \bar{x}_u^2} \tag{37}$$

The expression of $K_2(\bar{t})$ (renamed afterwards as $K(\bar{t})$) requires the value of $f_1(\bar{y}, \bar{t})$, which is governed by eqn (31b) subject to the conditions (32) and (33). Thus, to evaluate the cross-sectional averaged concentration of the solute, one need to calculate $f_1(\bar{y}, \bar{t})$. It may be noted that under the AC field based EOF, we may write $\bar{u}(\bar{y}, \bar{t}) = \Re\{\bar{u}_0(\bar{y}) \exp(-i\bar{\omega}\bar{t})\}$, where $\bar{\omega} = \omega H^2 / D_0$ and $\bar{u}_m(\bar{t}) = \Re\{\bar{u}_m \exp(-i\bar{\omega}\bar{t})\}$. With the same analogy we may further rewrite $f_1(\bar{y}, \bar{t}) = \Re\{F(\bar{y}) \exp(-i\bar{\omega}\bar{t})\}$. Substituting the same into (31a), (32) and (34) we may formulate the boundary value problem involving $F(\bar{y})$, and the same is summarized below

$$F''(\bar{y}) - n^2 F(\bar{y}) = \bar{u}_0(\bar{y}) - \bar{u}_m \tag{38}$$

subject to the boundary conditions

$$\left.\frac{\mathrm{d}F}{\mathrm{d}\bar{y}}\right|_{\bar{y}=-1} = 0 \tag{39a}$$

$$F\{(-1 + \bar{\delta})^-\} = F\{(-1 + \bar{\delta})^+\} \tag{39b}$$

$$\left.\frac{\mathrm{d}F}{\mathrm{d}\bar{y}}\right|_{\bar{y}=(-1+\bar{\delta})^-} = \left.\frac{\mathrm{d}F}{\mathrm{d}\bar{y}}\right|_{\bar{y}=(-1+\bar{\delta})^+} \tag{39c}$$

$$\left.\frac{\mathrm{d}F}{\mathrm{d}\bar{y}}\right|_{\bar{y}=0} = 0 \tag{39d}$$

where $n = \sqrt{-i\bar{\omega}}$. Solving (38) subject to the boundary conditions (39a)–(39d) yields

$$F(\bar{y}) = \begin{cases} D_1 \cosh(n\bar{y}) + D_2 \sinh(n\bar{y}) + \dfrac{1}{2n}[\exp(n\bar{y})J_5(\bar{y}) - \exp(-n\bar{y})J_6(\bar{y})]; & -1 < \bar{y} \leq -1 + \bar{\delta} \\[2mm] D_3 \cosh(n\bar{y}) + D_4 \sinh(n\bar{y}) + \dfrac{1}{2n}[\exp(n\bar{y})J_7(\bar{y}) - \exp(-n\bar{y})J_8(\bar{y})]; & -1 + \bar{\delta} < \bar{y} \leq 0 \end{cases} \tag{40}$$

The above expression (40) contains the constants D_i ($i = 1, 2, 3, 4$) and integrals $J_i(\bar{y})$ ($i = 5, 6, 7, 8$), which are summarized in Appendix-A.

The relation for dispersion coefficient $K(\bar{t})$ may be written in terms of $F(\bar{y})$ and is given below

$$K(\bar{t}) = \frac{1}{\mathrm{Pe}^2} - \int_{-1}^{0} (\Re\{\bar{u}_0(\bar{y}) \exp(-i\bar{\omega}\bar{t})\}$$
$$- \Re\{\bar{u}_m \exp(-i\bar{\omega}\bar{t})\})\Re\{F(\bar{y}) \exp(-i\bar{\omega}\bar{t})\}\mathrm{d}\bar{y} \tag{41}$$

We further introduce a new time dependent variable $\xi(\bar{t})$, defined as

$$\xi(\bar{t}) = \int_0^{\bar{t}} K(\tau)\mathrm{d}\tau \tag{42}$$

Note that $\sqrt{2\xi(\bar{t})}$ indicates the standard deviation of distribution of $\bar{C}_m$ at a given time $\bar{t}$. Such a quantity measures the width of the dispersed zone of the solutes. Using the above transformation (42), we may transform eqn (37) and the associated initial and boundary conditions as follows

$$\frac{\partial \bar{C}_m}{\partial \xi} = \frac{\partial \bar{C}_m^2}{\partial \bar{x}_u^2} \tag{43}$$

subject to

$$\bar{C}_m(\bar{x}_u, 0) = 2\bar{L}\delta_{\bar{L}}, \quad \bar{C}_m(\pm\infty, \bar{t}) = 0 \tag{44}$$

where

$$\delta_{\bar{L}} = \begin{cases} 1/(2\bar{L}), & \text{when } |x| \leq \bar{L} \\ 0, & \text{when } |x| > \bar{L} \end{cases} \tag{45}$$

Using the Fourier transformation, we can easily transform eqn (43) and (44) into the following equations

$$\frac{\partial \tilde{\bar{C}}_m}{\partial \xi} = -\bar{\omega}^2 \tilde{\bar{C}}_m \tag{46}$$

and,

$$\tilde{\bar{C}}_m(\bar{\omega}, 0) = \int_{-\infty}^{+\infty} 2\bar{L}\delta_{\bar{L}} \exp(-i\bar{\omega}\bar{x}_u)\mathrm{d}\bar{x}_u \tag{47}$$

where $\tilde{\bar{C}}_m(\bar{\omega}, \xi) = \int_{-\infty}^{+\infty} \bar{C}_m(\bar{x}_u, \xi) \exp(-i\bar{\omega}\bar{x}_u)\mathrm{d}\bar{x}_u$, and $\bar{\omega}$ represents the scaled spatial wave number, defined earlier. The solution of eqn (46) subject to conditions indicated in (47) is given as follows

$$\tilde{\bar{C}}_m(\bar{\omega}, \xi) = \tilde{\bar{C}}_m(\bar{\omega}, 0) \exp(-\bar{\omega}^2 \xi)$$
$$= \exp(-\bar{\omega}^2 \xi) \int_{-\infty}^{+\infty} 2\bar{L}\delta_{\bar{L}} \exp(-i\bar{\omega}\bar{x}_u)\mathrm{d}\bar{x}_u \tag{48}$$

Using inverse Fourier transform on the function $\tilde{\bar{C}}_m(\bar{\omega}, \xi)$, we may deduce the time evolution of the spatially dependent area-averaged solute concentration as follows

$$\bar{C}_m(\bar{x}_u, \xi) = \frac{1}{2\pi}\int_{-\infty}^{+\infty} \tilde{\bar{C}}_m(\bar{\omega}, \xi) \exp(i\bar{\omega}\bar{x}_u)\mathrm{d}\bar{\omega}$$
$$= \frac{1}{2}\left\{\mathrm{erf}\left(\frac{\bar{x}_u + \bar{L}}{2\sqrt{\xi}}\right) - \mathrm{erf}\left(\frac{\bar{x}_u - \bar{L}}{2\sqrt{\xi}}\right)\right\}. \tag{49}$$

where $\mathrm{erf}(\chi)$ indicates the error function, defined as $\mathrm{erf}(\chi) = \frac{2}{\sqrt{\pi}}\int_0^{\chi}\exp(-z^2)\mathrm{d}z$. It is worth noting that the quantities which provide the measurement of the dispersion process are $\bar{C}_m(\bar{x}_u, \bar{t})$, $K(\bar{t})$ and $\sqrt{2\xi(\bar{t})}$, respectively. In addition, we have further indicated the results for time-averaged effective dispersion coefficient K_{avg} over one oscillation period $\tau_0 = 2\pi/\omega$, defined as

$$K_{avg} = \frac{1}{\tau_0}\int_{\bar{t}}^{\bar{t}+\tau_0} K(t)\mathrm{d}t \tag{50}$$

In order to obtain the aforesaid quantities, the main input is the axial velocity profile and the method to deduce the same is already indicated. To obtain the dispersion coefficient $K(\bar{t})$, we need to calculate the function $F(\bar{y})$ using the closed form relation (40), which further involves the axial velocity. Note that the main complexity to deduce $F(\bar{y})$ is to calculate the integrals J_i ($i = 5, 6, 7, 8$), which are calculated using MATHEMATICA software. With the known values of axial velocity and $F(\bar{y})$, the relation (41) is implemented to calculate $K(\bar{t})$. The relations (42), (49) and (50) are further implemented to derive the results for $\sqrt{2\xi(\bar{t})}$, $\bar{C}_m(\bar{x}_u, \bar{t})$ and K_{avg}, respectively.

It is noteworthy to mention that within the Debye–Hückel electrostatic framework and the limit of $\omega \to 0$ we have further deduced the closed form analytical results for all the quantities associated with the dispersion process, e.g., $\sqrt{2\xi(\bar{t})}$, $\bar{C}_m(\bar{x}_u, \bar{t})$ and K_{avg}, respectively. The detailed description of the same is further summarized in Appendix-D. In addition, we have further performed the validation of numerical quantities associated with the dispersion process with the aforesaid analytical results. The readers are referred to Appendix-D for more details related to the same.

4 Results and discussion

The main objective of the present study is to provide a quantitative measurement of the modulation EOF under an AC electric field in a channel filled with an electrolyte solution surrounded by a layer of a dielectric liquid. In addition to that, we further investigate the impact of flow of the background fluidic medium on the dispersion of the solute across such a channel. The pertinent parameters that affect the fluid flow and thereby the dispersion process are dielectric permittivity, viscosity and thickness of the dielectric liquid layer, electrolyte concentration, ion size, concentration of additional mobile ions present within the liquid layer, interfacial surface charge along the liquid–liquid interface, channel height, frequency of the applied electric field, *etc.* For solute dispersion, another additional intrinsic parameter is mass diffusivity of the solute. As indicated earlier, the dielectric permittivity of the membrane layer is in general lower than that of the electrolyte medium. We have varied systematically the dielectric constant of the membrane layer to account for the ion partitioning effect. Besides, the ion steric effect further plays a prominent role in the flow modulation specially for the case when the electrostatic charge carried by the considered fluidic system (*i.e.*, interfacial charge and molar concentration of additional mobile ions of the dielectric liquid layer) is moderate to high. The impact of the steric effect depends on the finite size of ions and electrolyte concentration, which we have varied systematically to produce the results for flow field and thereby the solute dispersion. For the EOF under AC electric field, the oscillating Reynolds number $Re_j = \tilde{\rho}_j \omega H^2 / \eta_j$ dictates the back and forth motion of the background medium, where the subscript $j = d$ or e is associated with the dielectric liquid layer or the electrolyte medium, respectively. We present the results for various choices of the channel height and frequency of the applied AC electric field.

Unless stated otherwise, the dielectric liquid which surrounds the electrolytic solution is considered as the oily organic solvent cyclohexyl bromide (CHB) for which the dielectric constant $\epsilon_d = 7.9 \times 8.854 \times 10^{-12} F \, m^{-1}$, viscosity $\eta_d = 2.269$ mPa s and mass density $\tilde{\rho}_d = 1345$ kg m^{-3}, respectively.[101] For such a choice of liquid layer, the viscosity ratio $\eta_R = 2.54$, dielectric permittivity ratio $\epsilon_R = 0.1$ and the interfacial tension is 9.2×10^{-3} N m^{-1}, respectively. The electric strength of electric field E_0 is taken as $E_0 = 10^3$ V m^{-1}. Thus, the Capillary number Ca $\ll$ 1. In addition to the CHB solvent, we have further presented the results changing suitably the dielectric permittivity as well as viscosity of the liquid layer adjacent to the supporting walls. For each of the cases, we found the Capillary number is far smaller than unity. A relatively broad range in frequency $\omega/2\pi$ is considered, *e.g.*, 10^5 Hz to 10^8 Hz, and such choices of frequency are rather common in the AC electric field driven EOF.[102,103]

4.1 Modulation of EOF

To illustrate the impact of pertinent parameters on the flow modulation we present the results for dimensionless velocity amplitude $|\bar{u}_0(\bar{y})|$. In Fig. 2 we have shown the results to discuss the impact of the Debye–Hückel parameter of κH with fixed ion size $r = 3.3$ Å (Fig. 2a) and the ion steric effect with fixed κH (Fig. 2b). The dielectric liquid which surrounds the electrolytic solution is considered as oily organic solvent cyclohexyl bromide (CHB). Choice of such a liquid in the layer adjacent to the supporting walls is reasonable as its dielectric permitivity is much lower than that of the aqueous medium and the liquid in adjacent phases in immiscible in nature. Thus, for the considered two-phase fluidic system, the ion partitioning effect arises due to a significant difference in dielectric permittivity of both the phases. Since the viscosity of the CHB solvent is high compared to that of the aqueous medium, the magnitude of
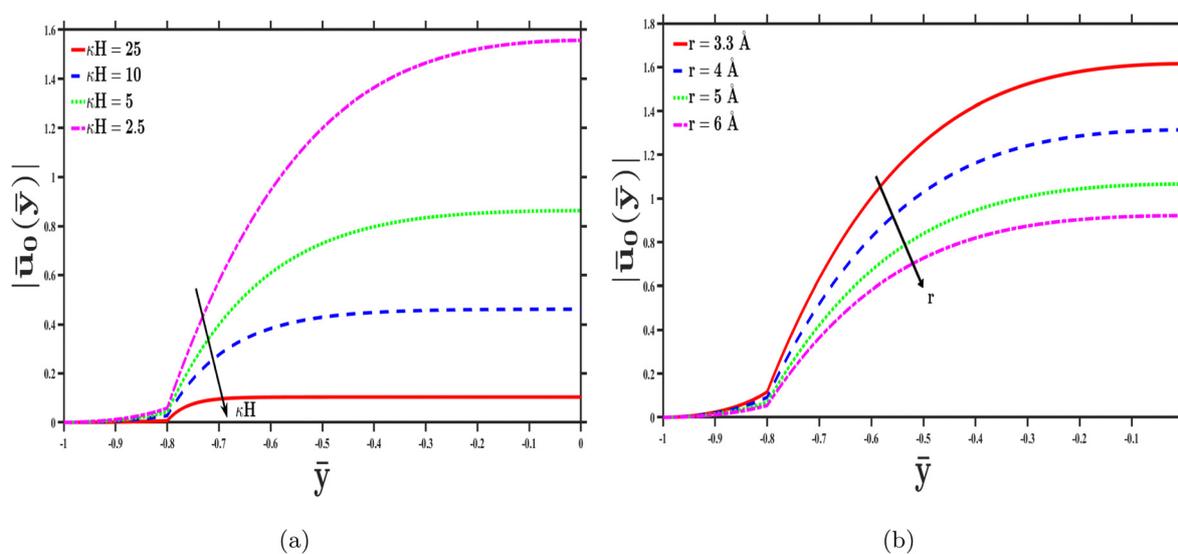

(a)

(b)

Fig. 2 The results for scaled velocity amplitude $|\bar{u}_0(\bar{y})|$ are shown for various values of (a) κH (= 2.5, 5, 10, and 25) with fixed $r = 3.3$ Å and (b) r (= 3.3 Å, 4 Å, 5 Å, and 6 Å) with fixed $\kappa H = 2.5$. The results are presented for fixed $H = 25$ nm, $\delta = 5$ nm, $N_0 = 1$ mM, $\bar{\sigma} = 2$ and $\bar{\omega} = 10$ (*i.e.*, $\omega/2\pi = 2.5 \times 10^6$ Hz), respectively.

$|\bar{u}_0(\bar{y})|$ within the liquid layer is substantially small compared to that in the electrolyte phase. We further observed that the strength of flow field reduces with the increase in κH (Fig. 2a). The accumulation of counterions near the charged interface enhances with the increase in κH, and thus, the impact of effective interfacial charge reduces, which leads to a significant reduction in flow strength. We observed that the velocity amplitude reduces with the increase in the size of electrolyte ions (Fig. 2b). In general, the finite sized ion restricts the accumulation of arbitrary number of counterions near the charged interface as well within the dielectric liquid layer. On the other hand, the increase in the ion size reduces the impact of the dielectric-gradient mediated ion partitioning effect. Combination of these two effects reduces the net neutralization mobile charge entrapped within the dielectric liquid layer, which enhances with the increase in the ion size and leads to a reduction in net electromotive force. As a result, the velocity amplitude $|\bar{u}_0(\bar{y})|$ reduces with increasing ion size.

In Fig. 3, we have shown the results for the velocity amplitude considering different values of dielectric permittivity and viscosity of the liquid in the layer adjacent to the supporting walls. We present the results for various choices of ϵ_R with fixed viscosity $\eta_R = 2.54$ (Fig. 3a) and in Fig. 3b we have shown the results for various choices of η_R with fixed dielectric permittivity $\epsilon_R = 0.1$. The results are presented for fixed values of other model parameters, which are summarized in the figure caption. As indicated earlier for CHB solvent $\epsilon_R = 0.1$ and $\eta_R = 2.54$, which is taken as the base value and an increase in ϵ_R and η_R indicates that the liquid in the dielectric layer is more polarizable in response to an electric field and more viscous compared to the CHB solvent, respectively. Besides, the increase in ϵ_R with fixed dielectric constant of the aqueous medium leads to an increase in dielectric permittivity of the liquid in the

layer adjacent to the channel wall. Thus, the impact of ion partitioning reduces, which in turn allows the accumulation of more counterions within the dielectric liquid layer. As a result, the neutralization of effective charge inside the liquid layer enhances and leads to a reduction in velocity amplitude $|\bar{u}_0(\bar{y})|$. As expected the velocity amplitude $|\bar{u}_0(\bar{y})|$ reduces with the increase in viscosity of the liquid layer adjacent to the supporting walls. Note that the increase in velocity amplitude $|\bar{u}_0(\bar{y})|$ within the liquid layer with its lower viscosity leads to an enhancement in $|\bar{u}_0(\bar{y})|$ within the aqueous phase so as to satisfy the continuity in flow velocity along the liquid–liquid interface.

In Fig. 4, we have presented the cross-sectional averaged velocity amplitude $|u_m|/U_{HS}$ (in the scaled form) as a function of Debye–Hückel parameter κH and dielectric permittivity ratio ϵ_R. The results are presented here for various choices of ion size. Other model parameters for Fig. 4 are summarized in the figure caption. The impact of the ion size on overall flow modulation is prominent for lower ranges of κH and ϵ_R. An increase in κH for a fixed channel height strengthens the shielding effect and thus leads to an enhanced charge neutralization. Besides, an increase in ϵ_R reduces the impact of the ion partitioning effect and thus enhances the accumulation of counterions within the liquid layer as well as near the charged interface. Thus, for a smaller range of κH or ϵ_R where the net charge of the fluidic system is high, the impact of the ion steric effect is prominent. However, its impact gradually diminishes with the increase in κH and ϵ_R. As expected the increase in the ion size reduces the net throughput due to the enhanced impact of the ion partitioning effect.

In Fig. 5 we have shown the results for dimensionless velocity amplitude $|\bar{u}_0(\bar{y})|$ for different values of interfacial charge $\bar{\sigma}$ (Fig. 5a), molar concentration N_0 of additional mobile ions within the membrane layer (Fig. 5b) and its thickness $\bar{\delta}$
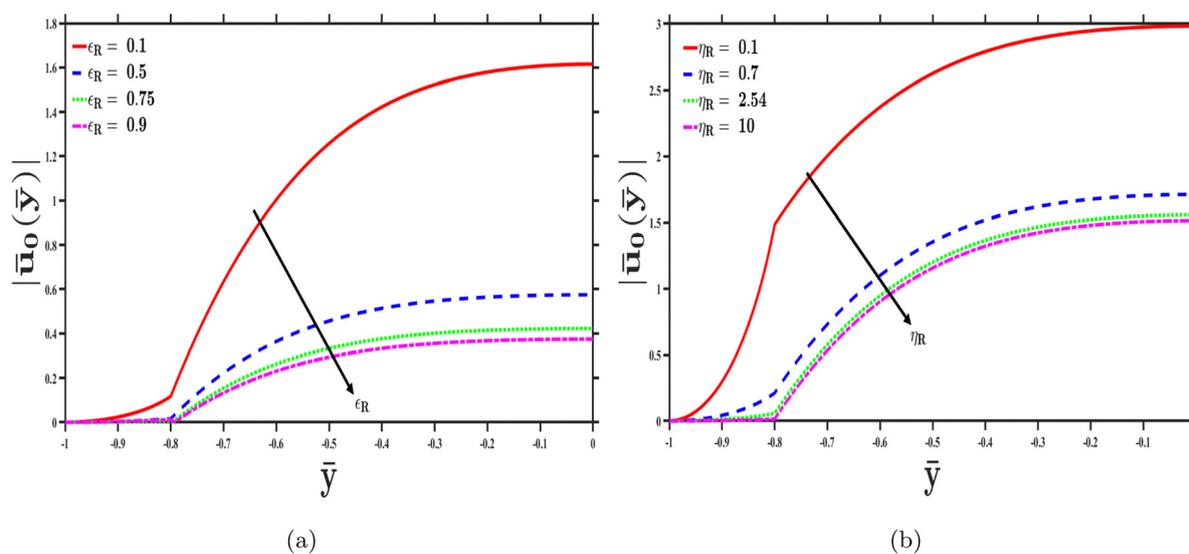

(a)

(b)

Fig. 3 The results for scaled velocity amplitude $|\bar{u}_0(\bar{y})|$ are shown for various values of (a) ϵ_R (= 0.1, 0.5, 0.75, and 0.9) with fixed $\eta_R = 2.54$ and (b) η_R (= 0.1, 0.7, 2.54, and 10) with fixed $\epsilon_R = 0.1$. Other model parameters are $H = 25$ nm, $\kappa H = 2.5$, $\delta = 5$ nm, $N_0 = 1$ mM, $\rho_R = 1.35$, $r = 3.3$ Å, $\bar{\sigma} = 2$, $\bar{\omega} = 10$.
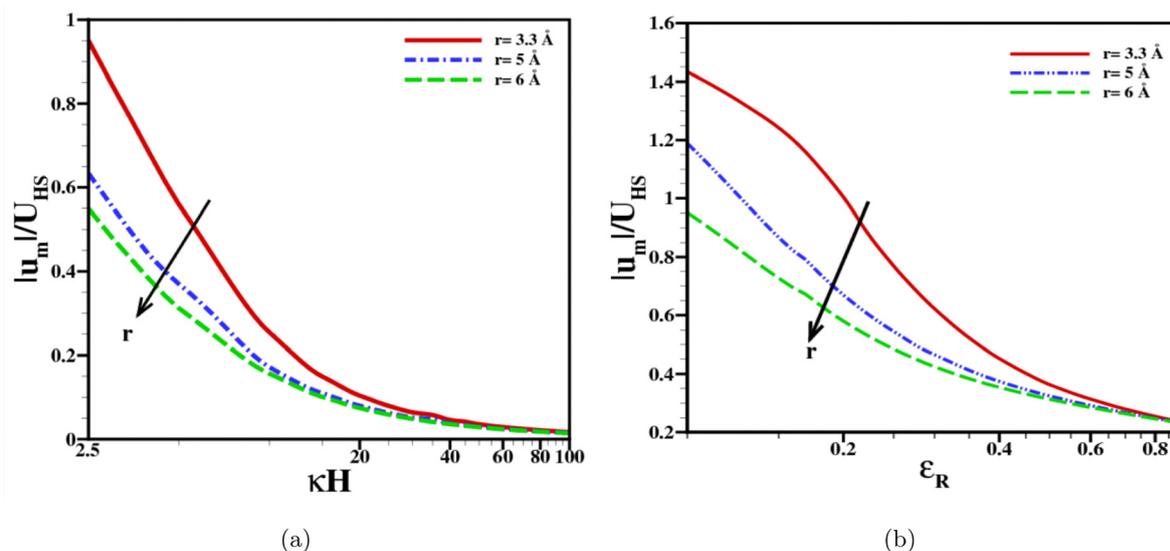
Fig. 4 The results for scaled cross-sectional averaged velocity amplitude $|u_m|/U_{HS}$ are shown as a function of (a) Debye–Hückel parameter κH for various values of r (= 3.3 Å, 5 Å, and 6 Å) with fixed $\epsilon_R = 0.1$ and (b) dielectric permittivity ratio ϵ_R for various values of r (= 3.3 Å, 5 Å, and 6 Å) with fixed $\kappa H = 2.5$. Other model parameters are $\bar{\sigma} = 2$, $N_0 = 1$ mM, $H = 25$ nm, $\bar{\delta} = 0.2$, $\rho_R = 1.35$, $\eta_R = 2.54$, $\bar{\omega} = 10$, respectively.
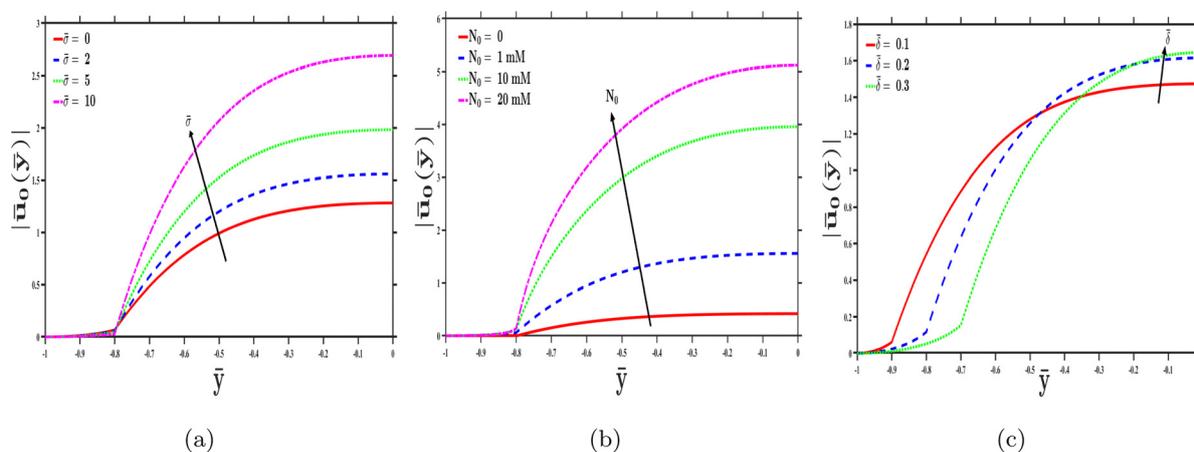
Fig. 5 The results for scaled velocity amplitude $|\bar{u}_0(\bar{y})|$ for various values of (a) $\bar{\sigma}$ (= 0, 2, 5, and 10) with fixed $N_0 = 1$ mM, $\delta = 5$ nm; (b) N_0 (= 0, 1 mM, 10 mM, and 20 mM) with fixed $\bar{\sigma} = 2$, $\delta = 5$ nm; and (c) δ (= 2.5 nm, 5 nm, and 7.5 nm) with fixed $\bar{\sigma} = 2$, $N_0 = 1$ mM. The results are shown here considering fixed values of other model parameters, *e.g.*, $H = 25$ nm, $\kappa H = 2.5$, $r = 3.3$ Å and $\bar{\omega} = 10$, respectively.

(Fig. 5c). Rise in interfacial charge density for fixed values of N_0 and $\bar{\delta}$ leads to an enhanced electrostatic potential in the membrane layer as well as in the aqueous medium and thus leads to an enhanced throughput. The impact of interfacial charge on the overall flow modulation further augments with the increase in N_0 and $\bar{\delta}$. Note that the increase in both of these quantities enhances the net effective charge density entrapped in the membrane layer. In Appendix-E, we have further shown the results for electrostatic potential distribution as well as net charge density considering different values of concentration of mobile charges in the dielectric liquid layer. A detailed discussion on the same is made thereat. Thus, the effective electromotive force further enhances with the increase in N_0

and $\bar{\delta}$, which in turn leads to an enhanced velocity amplitude $|\bar{u}_0(\bar{y})|$. Unlike that increase in interfacial charge or N_0, an increase in δ further leads to an enhanced motion deterring drag force due to higher viscosity of the dielectric liquid layer. Thus, it is expected that the interfacial charge and N_0 have more impacts on the flow modulation compared to the thickness δ of the dielectric liquid layer.

Fig. 6 further shows the impact of the channel height and frequency of the applied oscillatory electric field on the overall flow modulation. Note that these two parameters are directly related to the oscillating Reynolds number. As expected, with the increase in the channel height with fixed value of the scaled thickness of the dielectric liquid layer and other model
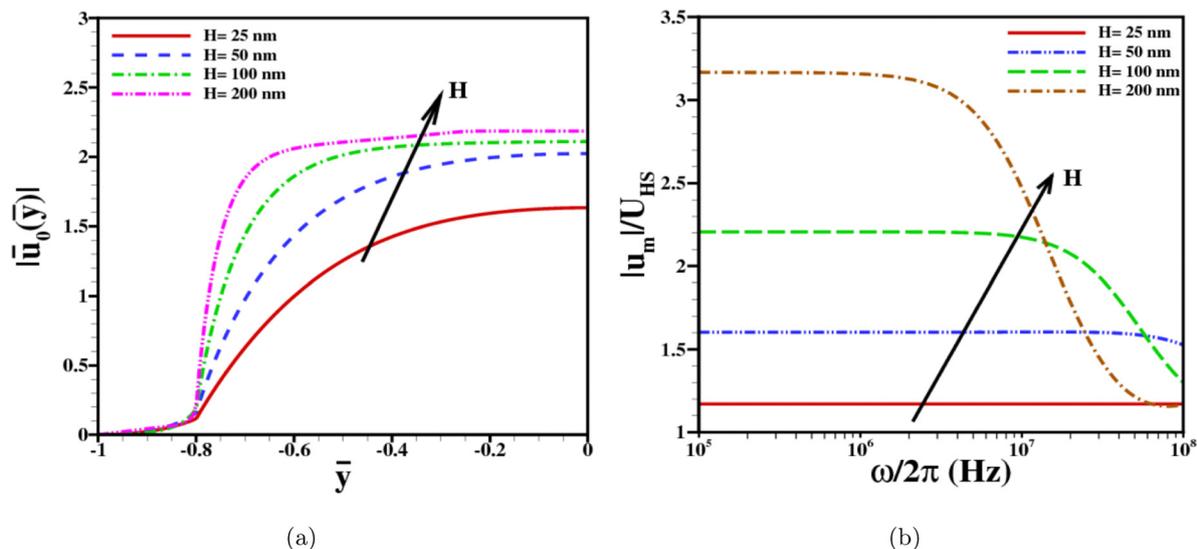
Fig. 6 (a) Scaled velocity amplitude $|\bar{u}_0(\bar{y})|$ is shown for various values of H (= 25 nm, 50 nm, 100 nm, and 200 nm) with fixed $\bar{\omega}$ = 10 (i.e., $\omega/2\pi$ = 2.5×10^6 Hz) and (b) scaled cross-sectional averaged velocity amplitude $|u_m|/U_{HS}$ is shown as a function of frequency $\omega/2\pi$ (Hz) for various values of H (= 25 nm, 50 nm, 100 nm, and 200 nm). The results are shown here considering the fixed values of other model parameters, e.g., κH = 2.5, r = 3.3 Å, N_0 = 1 mM and $\bar{\delta}$ = 0.2, respectively.

parameters, the net charge carried by the system enhances and leads to an enhanced velocity amplitude $|\bar{u}_0(\bar{y})|$ (Fig. 6a). We have further shown the results for scaled and cross-sectional averaged velocity amplitude as a function of oscillating frequency and the results are shown for various channel heights (Fig. 6b). We observe that the impact of oscillating frequency on the flow modulation is significant when the channel height is large. The increase in oscillating frequency accelerates the back and forth motion of the fluid medium. At a smaller range in oscillating frequency, the average velocity amplitude increases with the increase in the channel height. However, the averaged velocity amplitude reduces with the increase in frequency of the applied oscillatory electric field and its impact is prominent for the channel with larger height. Note that unlike the DC-EOF, the background fluidic medium requires the transient time to respond to the AC electric field. Besides, the increase in ω enhances the oscillatory Reynolds number, which actually measures the relative importance of dynamic inertial force and viscous force. Thus, the increased impact of the inertial effect due to the increase in oscillatory frequency leads to a substantial reduction in the average velocity amplitude. The impact of the oscillatory frequency on the overall reduction in the average velocity amplitude is further augmented for channels with larger height for which the oscillatory Reynolds number is large.

From the results presented in Fig. 2–6 we have observed that a significant flow enhancement is possible for the electrolyte with low concentration (e.g., a lower range of κH) and small size of electrolyte ions. Besides, the choice of liquid in the layer adjacent to the walls further plays a significant role in the maximum throughput. For example, when the dielectric permittivity of the liquid layer is small compared to the liquid

layer, a significant flow modulation is possible. Furthermore the net effective charge of the liquid layer enhances the flow strength, which can be achieved by increasing thickness and the concentration of mobile charge of the said layer as well as the interfacial charge. In addition, the flow strength across the channel is high for a smaller range of frequencies of the oscillatory electric field, and a reduction in the average throughput is possible with the increase in frequency of the applied AC electric field. Next we have discussed the impact of the modulated flow field on the dispersion process considering various mass diffusivity of the solutes.

4.2 Dispersion of solutes

In this section we have illustrated the results to highlight the dispersion of the solute band placed initially along the middle of the channel with a given bandwidth $2\bar{L}$ = 0.2 (in the scaled form). The band of solutes was dispersed due to molecular diffusion and fluid convection was induced by an applied oscillatory electric field. Note that the mass diffusivity of the uncharged solutes in general ranges from 10^{-12} m^2 s^{-1} to 10^{-9} m^2 s^{-1}.[104] Thus, for the considered flow geometry with a given channel height, the Péclet number (Pe) associated with the dispersion process ranges from 0.05 to 50. To analyze the findings related to solute dispersion we present the results for time evolution of cross-sectional averaged solute concentration $\bar{C}_m$, effective dispersion coefficient $K(\bar{t})$, standard deviation $\sqrt{2\xi(\bar{t})}$ of the distribution of $\bar{C}_m$ and time-averaged effective dispersion coefficient K_{avg} over one oscillation period $\tau_0 = 2\pi/\omega$, respectively.

To start with, we have first presented the results for time evolution of the cross-sectional averaged solute concentration
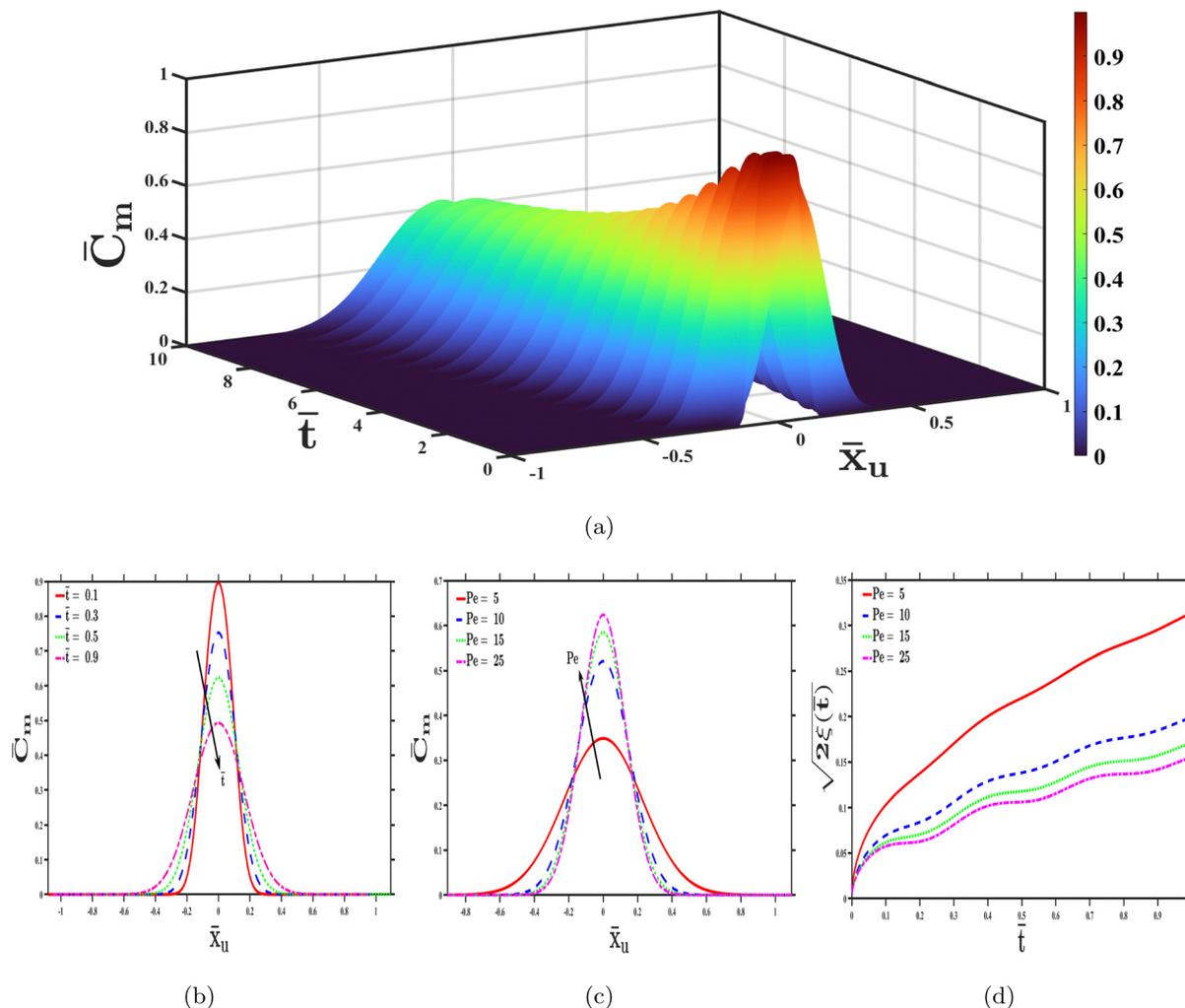
Fig. 7 (a) The time evolution of cross sectional averaged mean concentration distribution $\bar{C}_m$ is shown as a function of moving co-ordinate system $\bar{x}_u$ and scaled time $\bar{t}$ for Pe = 25. (b) The time evolution of $\bar{C}_m$ for discrete values of time, *i.e.*, $\bar{t}$ (= 0.1, 0.3, 0.5, and 0.9) is further shown. (c) The results for $\bar{C}_m$ for various choices of Péclet number Pe (= 5, 10, 15, and 25) at a fixed time $\bar{t}$ = 0.5. (d) The results indicating the time evolution of $\sqrt{2\xi(\bar{t})}$ as a function of scaled time $\bar{t}$ for various values of Pe (= 5, 10, 15 and 25). The results are shown here considering fixed values of other model parameters, *e.g.*, r = 3.3 Å, H = 25 nm, κH = 2.5, δ = 5 nm, N_0 = 1 mM, $\bar{\sigma}$ = 2, $\bar{\omega}$ = 10 and $\bar{L}$ = 0.1, respectively.

$\bar{C}_m(\bar{x}_u, \bar{t})$. We have shown the results for time evolution of $\bar{C}_m(\bar{x}_u, \bar{t})$ at a fixed value of Pe = 25 (Fig. 7a). The corresponding line plots for $\bar{C}_m(\bar{x}_u, \bar{t})$ for discrete values of scaled time $\bar{t}$ are further shown in Fig. 7b. We observed that as the time grows, the dispersion of solutes under the combined impact of molecular diffusion and oscillatory convective effect increases and leads to a significant band broadening of the solute placed inside the channel. The impact of the Péclet number on the spatial distribution of averaged concentration $\bar{C}_m$ is shown in Fig. 7c, where we have presented the results indicating the line plots for $\bar{C}_m$ for various choices of Péclet numbers at a given time. In addition, we have further shown the results in Fig. S.1 (ESI†) to indicate the time evolution of $\bar{C}_m(\bar{x}_u, \bar{t})$ for various values of Pe, where the Péclet number is varied by suitably changing the mass diffusivity of the solutes with fixed values of other model parameters. For such cases, an increase in the

Péclet number indicates a reduction in mass diffusivity of the solutes. As expected the broadening is higher at smaller values of Pe due to enhanced mass diffusivity of the solutes. For such cases the molecular diffusion dominates over the convective dispersion process. The quantitative measurement of band broadening is dictated by the time evolution of standard deviation $\sqrt{2\xi(\bar{t})}$ of the distribution of $\bar{C}_m$, as presented in Fig. 7d. Such a quantity indicates the width of the sample zone at a specified time. The oscillatory behaviour of the time evolution of $\sqrt{2\xi(\bar{t})}$ is prominent for a larger range of Péclet numbers for which the oscillatory convection effect dominates over the diffusion process. However, the width of the sample zone is higher for small Péclet numbers due to a strong diffusion effect.

In Fig. 8–10 (and Fig. S.3–S.6 shown in the ESI†), we have presented the results to indicate the impact of pertinent

(a)

(b)
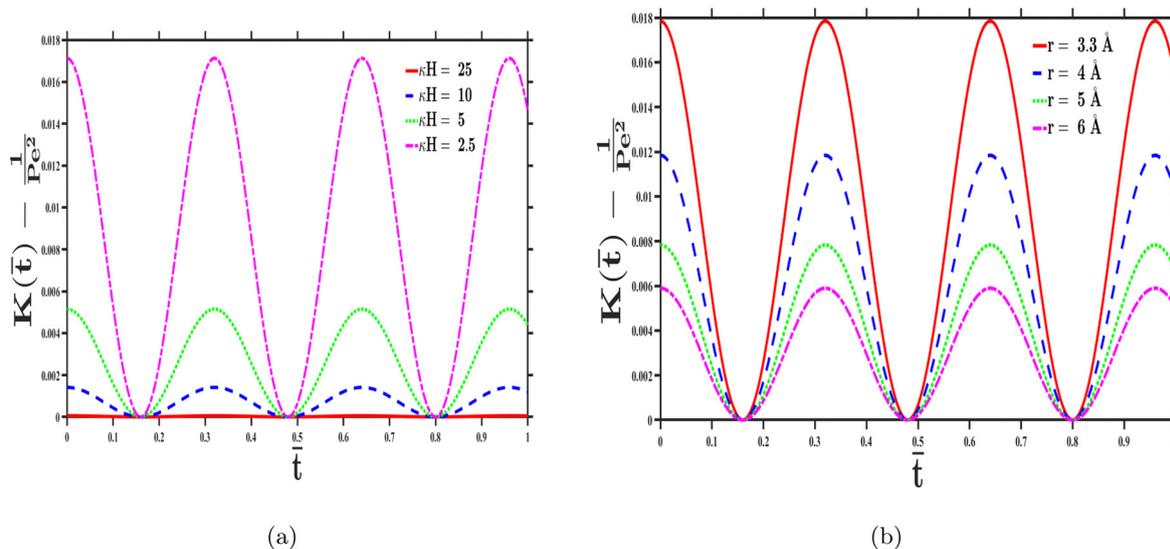
Fig. 8 Time periodic dispersion coefficients $K(\bar{t}) - 1/\text{Pe}^2$ are shown as a function of scaled time $\bar{t}$ for various values of (a) κH (= 2.5, 5, 10, and 25) with fixed r = 3.3 Å and (b) r (= 3.3 Å, 4 Å, 5 Å, and 6 Å) with fixed κH = 2.5. The results are presented here considering the fixed values of other model parameters, *e.g.*, H = 25 nm, δ = 5 nm, N_0 = 1 mM, $\bar{\sigma}$ = 2 and $\bar{\omega}$ = 10 and $\bar{L}$ = 0.1, respectively.

(a)

(b)
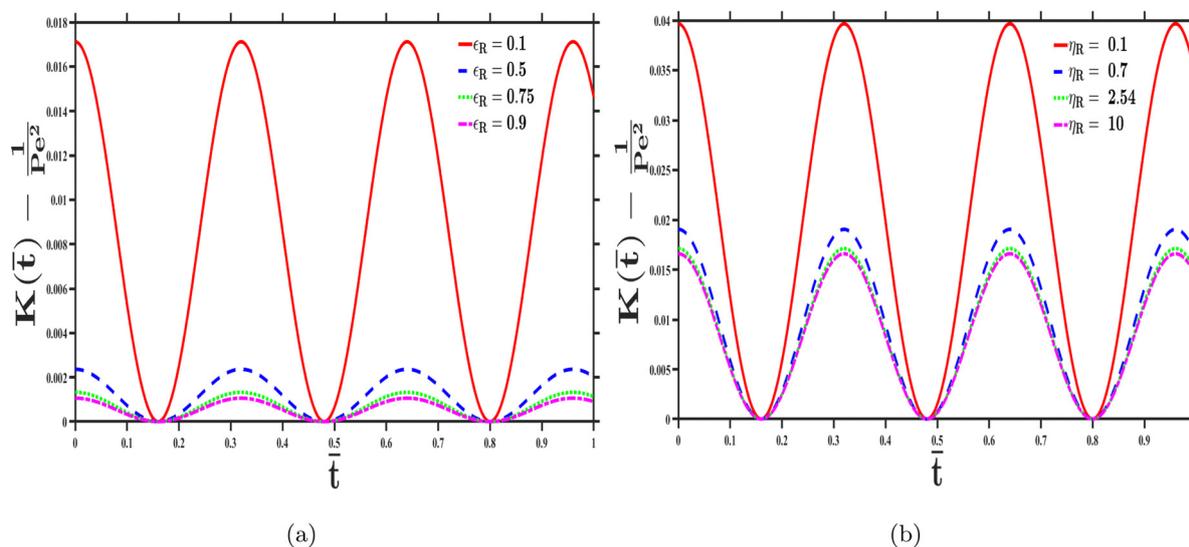
Fig. 9 Time periodic dispersion coefficients $K(\bar{t}) - 1/\text{Pe}^2$ are shown as a function of scaled time $\bar{t}$ for various values of (a) ϵ_R (= 0.1, 0.5, 0.75, and 1) with fixed η_R = 2.54 and (b) η_R (= 0.1, 0.7, 2.54, and 10) with fixed ϵ_R = 0.1. The results are presented here considering fixed values of other model parameters, *e.g.*, H = 25 nm, κH = 2.5, δ = 5 nm, N_0 = 1 mM, r = 3.3 Å, $\bar{\sigma}$ = 2, $\bar{\omega}$ = 10 and $\bar{L}$ = 0.1, respectively.

parameters associated with the flow modulation on the dispersion coefficient $K(\bar{t})$ (the influence of the axial diffusion $1/\text{Pe}^2$ is deduced). In Fig. 8 the results for $K(\bar{t}) - 1/\text{Pe}^2$ are presented for fixed Pe with a similar set of other model parameters as considered in Fig. 2. Impact of convective transport on the dispersion process is evident from the results presented in Fig. 8. As observed in Fig. 2, the velocity amplitude $|\bar{u}_0(\bar{y})|$ increases (decreases) with the increase in the EDL thickness (ion size). As a result the amplitude of the oscillatory dispersion coefficient increases with the reduction in κH (Fig. 8a), and it

reduces with the increase in the ion size (Fig. 8b). In addition, the oscillatory behavior of the dispersion coefficient enhances with the increase in the impact of fluid convection. In Fig. S.2 (ESI†) we have further shown the corresponding results for time evolution of $\sqrt{2\xi(\bar{t})}$ (Fig. S.2a and b, ESI†) and cross-sectional averaged $\bar{C}_m$ at a given time $\bar{t}$ = 0.5 (Fig. S.2c and d, ESI†) for different values of κH and ion size. The model parameters in Fig. S.2 (ESI†) are the same as considered in Fig. 8. It is evident that the band broadening is higher for the cases when the impact of fluid convection is strong. The larger dispersion
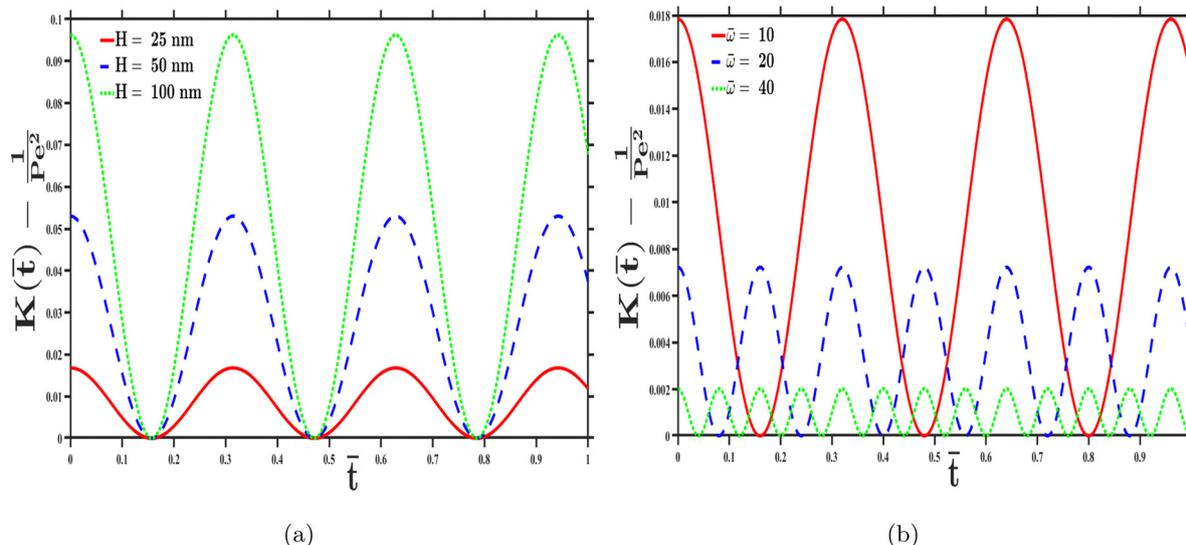
Fig. 10 Time periodic dispersion coefficients $K(\bar{t}) - 1/\text{Pe}^2$ are shown as a function of scaled time $\bar{t}$ for various values of (a) H (= 25 nm, 50 nm, and 100 nm) for fixed $\bar{\omega} = 10$ and (b) $\bar{\omega}$ (= 10, 20, and 40) for fixed H = 25. The results are presented here considering the fixed values of other model parameters, $e.g.$, r = 3.3 Å, N_0 = 1 mM, κH = 2.5 nm, $\bar{\delta}$ = 0.2, $\bar{\sigma}$ = 2, $\bar{\omega}$ = 10, and $\bar{L}$ = 0.1, respectively.

coefficient $K(\bar{t}) - 1/\text{Pe}^2$ is a direct consequence of the larger effective Péclet number based on the overall strength of the flow field with fixed molecular diffusion of solutes. Thus, the peak of mean concentration $\bar{C}_m$ decreases with the reduction in κH as well as with the reduction in the ion size for which the velocity amplitude $|\bar{u}_0(\bar{y})|$ is enhanced.

In Fig. 9, we have presented the results for $K(\bar{t}) - 1/\text{Pe}^2$ for various choices of dielectric permittivity ratios (ϵ_R) (Fig. 9a) and viscosity ratios (η_R) (Fig. 9) for fixed values of other model parameters. In addition, the time evolution of $\sqrt{2\xi(\bar{t})}$ and $\bar{C}_m$ at a given time $\bar{t}$ = 0.5 is presented in Fig. S.3 (ESI† for a similar set of pertinent parameters. As indicated earlier, the flow strength enhances with the reduction in ϵ_R (stated differently, an increase in the difference between the dielectric permittivity of both the phases or in other words, an increase in the ion partitioning effect). In addition, a reduction in viscosity of the liquid layer adjacent to the supporting walls further rises the velocity amplitude. Thus, the enhanced flow strength achieved in a smaller range of ϵ_R and η_R leads to a larger dispersion coefficient ($K(\bar{t}) - 1/\text{Pe}^2$) as well as a larger band broadening, which results in a smaller peak of the mean concentration. We further observed an enhanced dispersion of the solute band for increasing values of thickness and molar concentration of additional mobile ions present in the liquid layer adjacent to the supporting walls as well as interfacial charge density. The same is graphically illustrated in Fig. S.4 and S.5 (ESI†) which can further be justified with a similar analogy.

The dispersion coefficients $K(\bar{t}) - 1/\text{Pe}^2$ are further shown for various channel heights (Fig. 10a) and frequency of the oscillatory electric field (Fig. 10b). The results are presented here for the given value of other model parameters. As indicated earlier, an increase in the channel height leads to an enhanced flow rate. Thus, an enhanced dispersion coefficient

and a larger dispersion occur in the wider channel as a consequence of an enhanced effective Péclet number (Fig. 10a and Fig. S.6a, ESI†). As a result the peak of the mean concentration profile reduces with the increase in the channel height (Fig. S.6c, ESI†). We observe that the increase in oscillatory frequency reduces the effective dispersion coefficient (Fig. 10b), and results in a reduced bandwidth (Fig. S.6b, ESI†) and hence the larger peak in the mean solute concentration (Fig. S.6d, ESI†). Note that for higher frequency, the diffusion time is much higher than the oscillating period of applied AC electric field. Thus, the solute band does not have enough time to diffuse in a larger area. In addition, an increase in frequency and the increased inertia effect lead to a reduction in velocity amplitude. As a result the convective dispersion process with the increase in oscillatory frequency becomes weaker.

We have further presented the results for time-averaged effective dispersion coefficient K_{avg} over one oscillation period $\tau_0 = 2\pi/\omega$. Such a quantity is an important parameter to analyze the broadening of the solute band placed in an oscillatory flow field. In Fig. 11a–c we have shown the results for K_{avg} as a function of frequency of the applied oscillatory electric field. We present the results for various choices of κH (Fig. 11a), ion size (Fig. 11b) and dielectric permittivity ratio ϵ_R (Fig. 11c). Other model parameters are indicated in the caption of the said figure. As expected the time-averaged effective dispersion K_{avg} reduces with the increase in oscillatory frequency. Such a reduction is due to enhanced periodical expansion and contraction of the solute band placed under the oscillatory flow field. For a smaller range of oscillatory frequencies, due to an enhanced flow strength with reduction in κH, ion size as well as ϵ_R, the magnitude in K_{avg} increases. However, their impact on K_{avg} gradually diminishes with the increase in frequency of the oscillatory electric field. In Fig. S.7 (ESI†) we have further shown
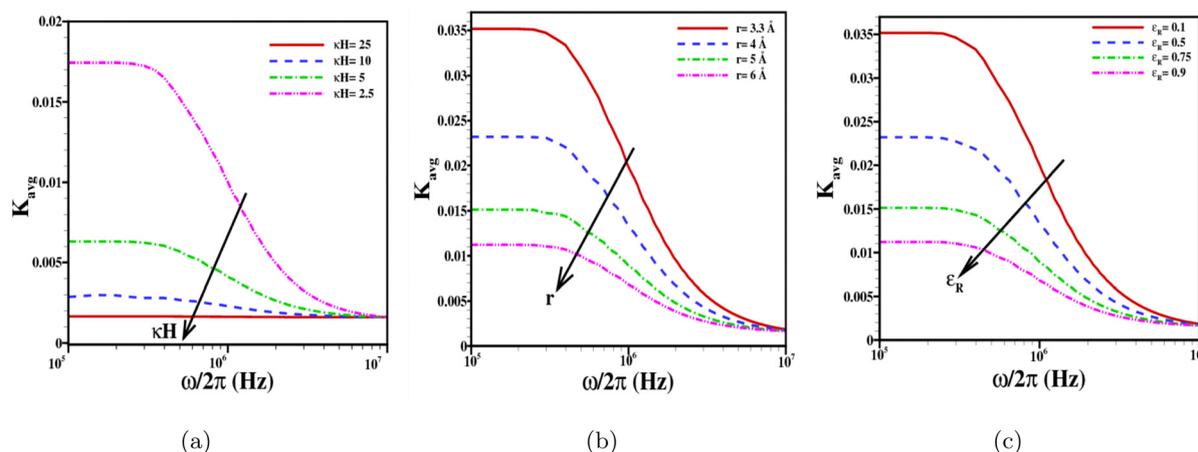
Fig. 11 Time average dispersion coefficient K_{avg} is shown as a function of frequency $\omega/2\pi$ (Hz) for various values of (a) κH (= 2.5, 5, 10, and 25) with fixed r = 3.3 Å, $\epsilon_R = 0.1$; (b) r (= 3.3 Å, 4 Å, 5 Å, and 6 Å) with fixed κH = 2.5, $\epsilon_R = 0.1$ and (c) ϵ_R (= 0.1, 0.5, 0.75, and 0.9) with fixed r = 3.3 Å, κH = 2.5. The results are presented for fixed H = 25 nm, δ = 5 nm, N_0 = 1 mM, $\rho_R = 1.35$, $\eta_R = 2.54$, Pe = 25 and $\bar{\sigma}$ = 2, respectively.

the impact of other pertinent parameters associated with flow modulation (*e.g.*, viscosity ratio η_R, thickness $\bar{\delta}$, interfacial charge $\bar{\sigma}$ and molar concentration N_0). The viscosity ratio η_R has little effect on the time-averaged effective dispersion K_{avg}, however, $\bar{\delta}$, $\bar{\sigma}$ and N_0 have a substantial impact on K_{avg}, when frequency of the oscillatory electric field is small. We observed that when $\omega/2\pi$ is smaller than 6×10^5 Hz, the impact of oscillatory electric field on the flow modulation, dispersion coefficient as well as band broadening is prominent. However, beyond this limit of frequency, an increase in oscillatory frequency ω reduces the impact of pertinent parameters on the flow modulation and hence the dispersion characteristics.

In Fig. 12, we have shown the results for time-averaged dispersion coefficient K_{avg} over one oscillation period as a function of oscillatory frequency and the results are shown here for various choices of Péclet number. We have systematically changed the Péclet number either by varying mass diffusivity with fixed channel height (Fig. 12a), or by varying the channel height at a given mass diffusivity (Fig. 12b) and the results are presented for fixed values of the other model parameters. As expected, a larger K_{avg} is achieved with large (small) values of mass diffusivity (Péclet number). The magnitude of K_{avg} further reduces with the increase in oscillatory frequency for which the impact of effective fluid convection reduces. We further observe an enhanced K_{avg} for
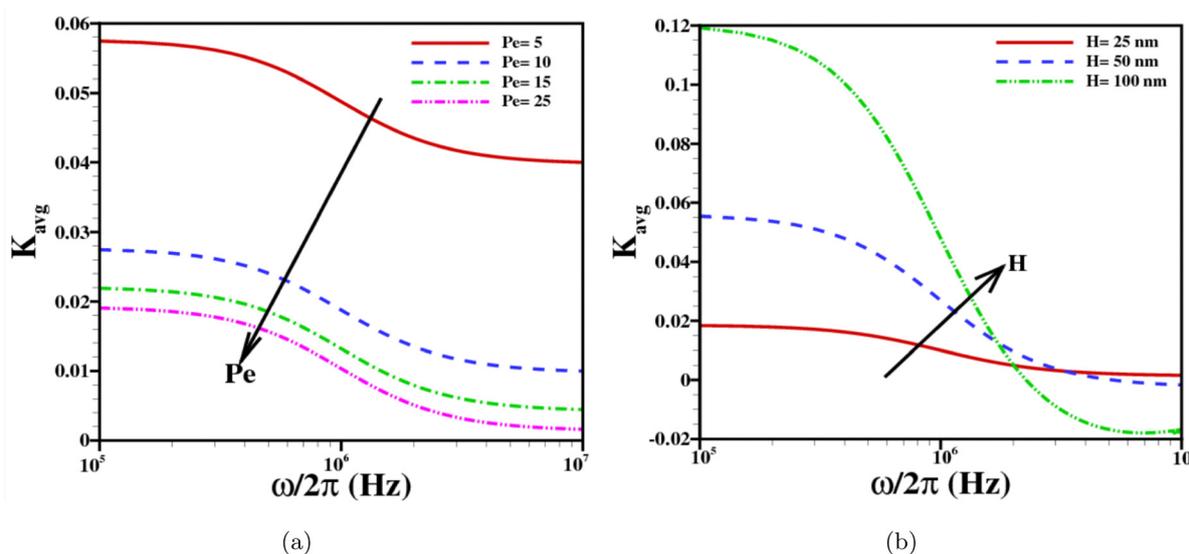
Fig. 12 The time-averaged effective dispersion coefficient K_{avg} over one oscillation period is shown as a function of frequency $\omega/2\pi$ (Hz) for various values of (a) Pe (= 5, 10, 15, and 25) with fixed channel height H = 25 nm and (b) H (= 25 nm, 50 nm, and 100 nm) with fixed mass diffusion coefficient $D_0 = 2.05 \times 10^{-10}$ m^2 s^{-1}. The results are presented here considering the fixed values of other model parameters, *e.g.*, r = 3.3 Å, N_0 = 1 mM, κH = 2.5, $\bar{\delta}$ = 0.2 and $\bar{\sigma}$ = 2, respectively.

an increasing channel height. The same is however possible due to the enhanced fluid convection effect, especially for a smaller range of oscillatory frequencies. Moreover, for the considered problem dealing with solute dispersion under AC EOF, a change in sign of K_{avg} is observed, especially for channels with a larger size and at larger oscillatory frequency. Note that the variance of the solute dispersion is always positive, however, it does not ensure that differential variance, referred to as the effective dispersion coefficient, remains always positive. The occurrence of the negative effective dispersion coefficient for oscillatory flow field is rather common.[55,105–107] As indicated earlier, the increase in the channel height results in an enhanced dispersion. The transition from the positive to negative value of K_{avg} is caused by a rapid change in periodical expansion and contraction of the solute band under EOF induced by an oscillatory electric field with large frequency.

5 Conclusion

The present article provides an extensive study on the modulation of EOF involving a two-phase liquid system under an oscillatory electric field and its impact on the transport and dispersion processes of the solute band placed along the middle of the channel. In the considered two-phase liquid system, the electrolyte medium is surrounded by a layer of a dielectric liquid, which resembles a membrane of biological cells containing additional mobile charges. The difference in dielectric permittivity of both the phases induces an ion partitioning effect, which plays a significant role in the flow modulation and therefore in solute dispersion. In addition, the ion steric effect comes into play, specifically when the charge carried by the system is moderate to high. We have presented the results for flow modulation under an applied AC electric field across such a channel and further studied the dispersion of the solute band. We measured the magnitude of complex amplitude of the velocity field as well as the cross-sectional averaged velocity to dictate the impact of pertinent parameters on the overall flow modulation. Besides, to provide quantitative measurement of the dispersion process, we deduce the results for the cross-sectional averaged concentration $\bar{C}_m$ of the solute band, standard deviation of distribution of $\bar{C}_m$, and the time dependent dispersion coefficient as well as the time-averaged effective dispersion coefficient over one oscillation period. The numerical results are presented for a wide range of pertinent parameters. Besides, benchmark analytical results within the Debye–Hückel electrostatic framework for EDL potential and EOF velocity are deduced. The numerical calculations should pave the way for novel AC electric field based EOF pumping mechanisms and therefore the band broadening process. In addition, we deduced the analytical results for the said quantities associated with the dispersion process under the Debye–Hückel limit with vanishing frequency of the AC electric field. These benchmark

theoretical results are however important for validation purposes of the numerical scheme adopted in this study as well as for future applications.

We observe an enhanced flow strength and band broadening when the difference in dielectric permittivity of both the phases is high for which the impact of the ion partitioning effect is prominent. Reduction in the effect of ion partitioning reduces the flow strength, and thus molecular diffusion dominates over the convective dispersion process. The size in mobile ions is further related to the ion partitioning effect. An increase in the ion size reduces the effective electromotive force and leads to a reduction in the flow rate and dispersion coefficient. An augmented flow strength and enhanced convective dispersion process are observed with the increase in interfacial charge, thickness and additional mobile charge of the dielectric liquid layer. The impact of the ion steric effect is further augmented when the net charge within the fluidic system is high. A rise in the electrolyte concentration leads to an enhanced shielding effect and leads to a reduced strength of flow field, and thus reduces the convective effect on the dispersion process. As expected, due to the enhanced effective Péclet number, an enhanced dispersion coefficient and larger dispersion occur in the wider channel. An increase in oscillatory frequency causes a reduction in velocity amplitude due to the increased inertia effect, and thus the convective counterpart of the dispersion coefficient reduces. We further witness the negative value of the dispersion coefficient for a large channel height and a large frequency of the dispersion coefficient.

Finally, the present article provides an improved theory of modulation of oscillatory electroosmotic flow and solute dispersion considering a planar liquid–liquid interface, which indicates the basic state of a general stability problem. In our subsequent article we aim to study the instabilities associated with two-layer EOF under an oscillatory electric field and the present study will be a benchmark for such future studies. Besides, the study of ICR considering a two-phase liquid in the presence of any sort of asymmetries along the lateral dimension may be an important topic of future research.

Data availability

The authors confirm that the data supporting the findings of this study are available within the article. Additional supporting data, such as numerical data corresponding to the data presented in the figures, are available upon request to the corresponding author.

Conflicts of interest

The authors report no conflict of interest.

Appendices

Appendix-A: summary of various constants appearing in the velocity field and $F(\bar{y})$

The expression (16) for velocity field presented in main article contains several constants, which are summarized below

$$
\begin{cases}
m_1 = \sqrt{\dfrac{-i\omega\tilde{\rho}_{\mathrm{d}}H^2}{\eta_{\mathrm{d}}}} \\[10pt]
m_2 = \sqrt{\dfrac{\epsilon_{\mathrm{R}}}{\eta_{\mathrm{R}}}} \\[10pt]
m_3 = \sqrt{\dfrac{-i\omega\tilde{\rho}_{\mathrm{e}}H^2}{\eta_{\mathrm{e}}}} \\[10pt]
C_1 = C_2\tanh(m_1) - m_2^2\bar{\psi}(-1)\mathrm{sech}(m_1) \\[8pt]
C_2 = \dfrac{\cosh(m_1)}{L_1}\big\{(N_{21} + N_{22} + N_{23})m_3\sinh(m_3(-1+\bar{\delta})) - (N_{11} + N_{12} + N_{13})\cosh(m_3(-1+\bar{\delta}))\big\} \\[10pt]
C_3 = \dfrac{1}{L_1}\big\{(N_{11} + N_{12} + N_{13})\sinh(m_1\bar{\delta}) - \eta_{\mathrm{R}}m_1(N_{21} + N_{22} + N_{23})\cosh(m_1\bar{\delta})\big\} \\[10pt]
C_4 = -\dfrac{m_3}{2}(J_3(0) + J_4(0)) \\[10pt]
J_1(\bar{y}) = \displaystyle\int_{-1}^{\bar{y}}\exp(-m_1 x)\bar{\psi}(x)\mathrm{d}x \\[10pt]
J_2(\bar{y}) = \displaystyle\int_{-1}^{\bar{y}}\exp(m_1 x)\bar{\psi}(x)\mathrm{d}x \\[10pt]
J_3(\bar{y}) = \displaystyle\int_{-1+\bar{\delta}}^{\bar{y}}\exp(-m_3 x)\bar{\psi}(x)\mathrm{d}x \\[10pt]
J_4(\bar{y}) = \displaystyle\int_{-1+\bar{\delta}}^{\bar{y}}\exp(m_3 x)\bar{\psi}(x)\mathrm{d}x
\end{cases}
\tag{A.1}
$$

Various constants appearing in the above relation (A.1) are summarized below

$$
\begin{cases}
N_{11} = -m_1\eta_{\mathrm{R}}\sinh(m_1(-1+\bar{\delta}))m_2^2\bar{\psi}(-1)\mathrm{sech}(m_1) \\[10pt]
N_{12} = \dfrac{(m_1 m_2)^2}{2}\eta_{\mathrm{R}}\big\{\exp(m_1(-1+\bar{\delta}))J_1(-1+\bar{\delta}) + \exp(-m_1(-1+\bar{\delta}))J_2(-1+\bar{\delta})\big\} \\[10pt]
N_{13} = \dfrac{(m_3)^2}{2}\cosh(m_3(-1+\bar{\delta}))(J_3(0) + J_4(0)) \\[10pt]
N_{21} = \dfrac{(m_1 m_2)^2}{2m_1}\big\{\exp(m_1(-1+\bar{\delta}))J_1(-1+\bar{\delta}) - \exp(-m_1(-1+\bar{\delta}))J_2(-1+\bar{\delta})\big\} \\[10pt]
N_{22} = (m_2^2 - 1)\bar{\psi}(-1+\bar{\delta}) - m_2^2\bar{\psi}(-1)\mathrm{sech}(m_1)\cosh(m_1(-1+\bar{\delta})) \\[10pt]
N_{23} = \dfrac{(m_3)^2}{2m_3}\sinh(m_3(-1+\bar{\delta}))(J_3(0) + J_4(0)) \\[10pt]
L_1 = -\eta_{\mathrm{R}}m_1\cosh(m_1\bar{\delta})\cosh(m_3(-1+\bar{\delta})) + m_3\sinh(m_1\bar{\delta})\sinh(m_3(-1+\bar{\delta}))
\end{cases}
\tag{A.2}
$$

The function $F(\bar{y})$ appearing in eqn (40) of the main article involves the following constants

$$
\begin{cases}
D_1 = \dfrac{\cosh(n)}{2n\sinh(n\bar{\delta})}[-R_{12} + R_{13}] \\[2mm]
D_2 = \dfrac{\sinh(n)}{2n\sinh(n\bar{\delta})}[-R_{12} + R_{13}] \\[2mm]
D_3 = \dfrac{1}{2n\sinh(n)}[R_{11} - [J_7(0) + J_8(0)]\cosh(n)] \\[2mm]
D_4 = -\dfrac{1}{2n}[J_7(0) + J_8(0)] \\[2mm]
J_5(\bar{y}) = \displaystyle\int_{-1}^{\bar{y}} \exp(-nz)(\bar{u}_0(z) - \bar{u}_m)\mathrm{d}z \\[2mm]
J_6(\bar{y}) = \displaystyle\int_{-1}^{\bar{y}} \exp(nz)(\bar{u}_0(z) - \bar{u}_m)\mathrm{d}z \\[2mm]
J_7(\bar{y}) = \displaystyle\int_{-1+\bar{\delta}}^{\bar{y}} \exp(-nz)(\bar{u}_0(z) - \bar{u}_m)\mathrm{d}z \\[2mm]
J_8(\bar{y}) = \displaystyle\int_{-1+\bar{\delta}}^{\bar{y}} \exp(nz)(\bar{u}_0(z) - \bar{u}_m)\mathrm{d}z
\end{cases}
\tag{A.3}
$$

Several constants appearing in (A.3) are summarized below

$$
\begin{cases}
R_{11} = \left[\exp(n(-1+\bar{\delta}))J_5(-1+\bar{\delta})\{\sinh(n\bar{\delta}) - \cosh(n\bar{\delta})\} - \exp(-n(-1+\bar{\delta}))J_6(-1+\bar{\delta})\{\sinh(n\bar{\delta}) + \cosh(n\bar{\delta})\}\right] \\[2mm]
R_{12} = \exp(n(-1+\bar{\delta}))J_5(-1+\bar{\delta}) + \exp(-n(-1+\bar{\delta}))J_6(-1+\bar{\delta}) \\[2mm]
R_{13} = \dfrac{1}{\sinh(n)}\{R_{11} - [J_7(0) + J_8(0)]\cosh(n)\}\sinh(n(-1+\bar{\delta})) - [J_7(0) + J_8(0)]\cosh(n(-1+\bar{\delta}))
\end{cases}
\tag{A.4}
$$

Appendix-B: approximate analytical results for EDL potential

The analytical results for scaled EDL potential may be deduced as follows

$$
\bar{\psi}(\bar{y}) =
\begin{cases}
\dfrac{1}{2F_2}(2F_2\bar{\psi}_{\mathrm{D}} - F_1) + \dfrac{1}{4F_2}h_2(\bar{\psi}(-1+\bar{\delta}))\exp(-\kappa_n H\{\bar{y} - (-1+\bar{\delta})\}) + \dfrac{F_1^2}{4F_2 h_2(\bar{\psi}(-1+\bar{\delta}))}\exp(\kappa_n H\{\bar{y} - (-1+\bar{\delta})\}) & -1 < \bar{y} \le -1 + \bar{\delta} \\[4mm]
2\coth^{-1}\left[\dfrac{h_1(\bar{\psi}(-1+\bar{\delta}))}{2}\exp(\kappa H\{\bar{y} - (-1+\bar{\delta})\}) + \dfrac{(1+P)}{2h_1(\bar{\psi}(-1+\bar{\delta}))}\exp(-\kappa H\{\bar{y} - (-1+\bar{\delta})\})\right] & -1+\bar{\delta} < \bar{y} \le 0
\end{cases}
\tag{B.1}
$$

The above expression involves the following constants

$$
\begin{cases}
\kappa_n = \kappa_1\sqrt{F_2}\,\mathrm{sgn}(\bar{\psi}(-1+\bar{\delta})) \\[2mm]
F_1 = 2(1+P)\sinh(\bar{\psi}_{\mathrm{D}}) - P\sinh(2\bar{\psi}_{\mathrm{D}}) - 2M \\[2mm]
F_2 = (1+P)\cosh(\bar{\psi}_{\mathrm{D}}) - P\cosh(2\bar{\psi}_{\mathrm{D}}) + MZ(1-\Omega)
\end{cases}
\tag{B.2}
$$

where $\bar{\psi}(-1+\bar{\delta})$ represents the scaled interfacial potential at the liquid–liquid interface $\bar{y} = -1 + \bar{\delta}$ (*i.e.*, at the liquid/liquid interface), and the functions $h_1(\bar{\psi}(-1+\bar{\delta}))$, $h_2(\bar{\psi}(-1+\bar{\delta}))$ are defined by

$$
\begin{cases}
h_1(\bar{\psi}(-1+\bar{\delta})) = \coth\left(\dfrac{\bar{\psi}(-1+\bar{\delta})}{2}\right) + \sqrt{\coth^2\left(\dfrac{\bar{\psi}(-1+\bar{\delta})}{2}\right) - (1+P)} \\[4mm]
h_2(\bar{\psi}(-1+\bar{\delta})) = 2\sqrt{F_2}\left\{F_1(\bar{\psi}(-1+\bar{\delta}) - \bar{\psi}_{\mathrm{D}}) + F_1(\bar{\psi}(-1+\bar{\delta}) - \bar{\psi}_{\mathrm{D}})^2\right\}^{1/2} + 2F_2(\bar{\psi}(-1+\bar{\delta}) - \bar{\psi}_{\mathrm{D}}) + F_1
\end{cases}
\tag{B.3}
$$

Note that the interfacial potential $\bar{\psi}(-1+\bar{\delta})$ and the Donnan potential $\bar{\psi}_{\mathrm{D}}$ are implicitly connected to each other. The implicit relationship between both of them may be deduced as follows

$$
\begin{aligned}
\frac{\bar{\sigma}}{(\kappa H)\sqrt{2}} &= \\
&-\mathrm{sgn}(\bar{\psi}(-1+\bar{\delta}))\sqrt{\epsilon_{\mathrm{R}}f}\Big[(1+P)\{\cosh(\bar{\psi}(-1+\bar{\delta})) - \cosh(\bar{\psi}_{\mathrm{D}})\} \\
&\quad -\frac{P}{4}\{\cosh(2\bar{\psi}(-1+\bar{\delta})) - \cosh(2\bar{\psi}_{\mathrm{D}})\} \\
&\quad +\frac{M}{Z}((1+\Omega)\{\exp(-Z[\bar{\psi}(-1+\bar{\delta}) - \bar{\psi}_{\mathrm{D}}]) - 1\} \\
&\quad -\frac{\Omega}{2}\{\exp(-2Z[\bar{\psi}(-1+\bar{\delta}) - \bar{\psi}_{\mathrm{D}}]) - 1\})\Big]^{1/2} \\
&\quad +\left[(\cosh(\bar{\psi}(-1+\bar{\delta})) - 1)\left\{1 - \frac{P}{2}(\cosh(\bar{\psi}(-1+\bar{\delta})) - 1)\right\}\right]^{1/2}
\end{aligned}
\tag{B.4}
$$

We adopt a suitable numerical scheme to deduce the interfacial potential from the relation (B.4) with the known Donnan potential. Note that the explicit form of Donnan potential is given in the relation (11) appearing in the main manuscript (MS). With the known interfacial potential as well as Donnan potential we further obtain the spatial distribution of EDL potential using the relation (B.1). We have now presented a comparison of EDL potential obtained from the numerical scheme indicated in the main manuscript (MS) and the results obtained in this section. In Fig. 13a we have shown the spatial distribution of the EDL potential in the scaled form for various choices of κH with fixed values of other model parameters. We have further presented the results for EDL potential for increasing molar concentration of additional ions present in the dielectric liquid layer (Fig. 13b). We observe a close agreement in the numerical results with deduced analytical results for EDL potential for any choices of Debye–Hückel parameter and concentration of additional ions present in the dielectric liquid layer.
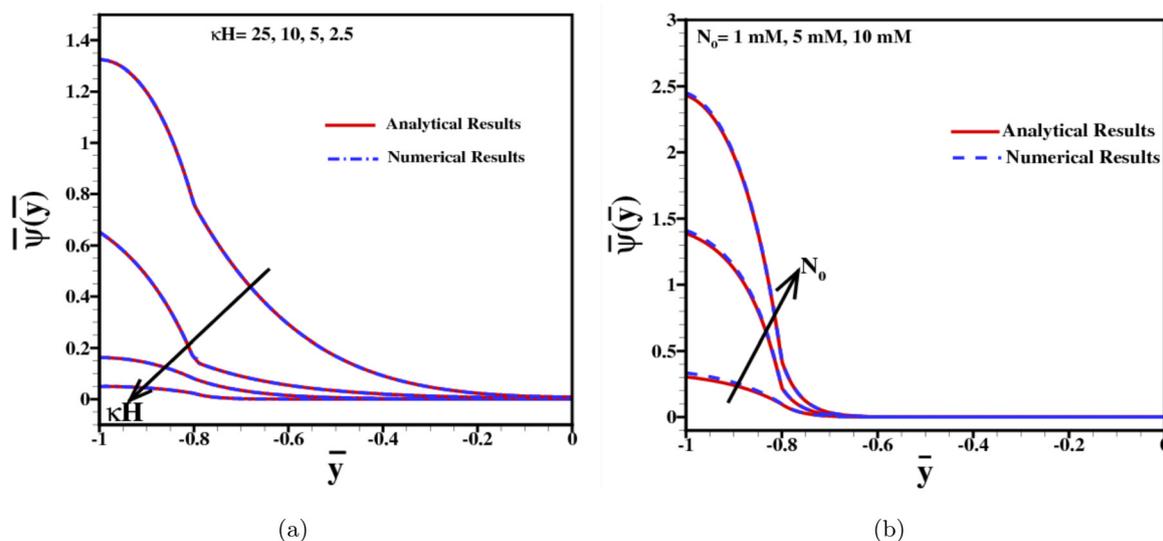
Fig. 13 Scaled potential distributions $\bar{\psi}(\bar{y})$ are shown as a function of scaled spatial coordinate $\bar{y}$ for various values of (a) κH (= 2.5, 5, 10, and 25) with fixed $N_0 = 1$ mM and (b) N_0 (= 1 mM, 5 mM, and 10 mM) with fixed $\kappa H = 25$. Other model parameters are $H = 25$ nm, $\delta = 5$ nm, $\bar{\sigma} = 2$, $\epsilon_R = 0.1$, and $r = 3.3$ Å, respectively.

Appendix-C: closed form analytical results for EDL potential and EOF field under the Debye–Hückel limit

Under the Debye–Hückel limit ($\bar{\psi}(\bar{y}) \ll 1$), the linearized form of the EDL potential equation (in the scaled form) may be written as

$$\frac{d^2\bar{\psi}}{d\bar{y}^2} = p_1{}^2\bar{\psi} - q_1 \qquad -1 < \bar{y} \leq -1 + \bar{\delta} \qquad \text{(C.1a)}$$

$$\frac{d^2\bar{\psi}}{d\bar{y}^2} = (\kappa H)^2\bar{\psi} \qquad -1 + \bar{\delta} < \bar{y} \leq 0. \qquad \text{(C.1b)}$$

where

$$\begin{cases} p_1 = (\kappa_1 H)\sqrt{1 + \dfrac{\bar{\psi}_D Z}{z}} \\[4mm] q_1 = \bar{\psi}_D(\kappa_1 H)^2\left(1 + \dfrac{\bar{\psi}_D Z}{z}\right) \end{cases} \qquad \text{(C.2)}$$

Solving the governing equations (C.1a) and (C.1b) subject to the boundary conditions (9a)–(9d) yields the explicit form of the EDL potential, given as

$$\bar{\psi}(\bar{y}) = \begin{cases} \dfrac{Q_1}{\cosh(p_1)}\cosh(p_1(\bar{y} + 1)) + \dfrac{q_1}{p_1{}^2}; & -1 < \bar{y} \leq -1 + \bar{\delta} \\[4mm] Q_2\cosh(\kappa H\bar{y}); & -1 + \bar{\delta} < \bar{y} \leq 0 \end{cases} \qquad \text{(C.3)}$$

where the constants Q_1 and Q_2 appearing in (C.3) are as follows

$$\begin{cases} Q_1 = \dfrac{\bar{\sigma}\cosh(\kappa H(-1 + \bar{\delta}))p_1{}^2 + (\kappa H)\sinh(\kappa H(-1 + \bar{\delta}))q_1}{-p_1{}^2(\kappa H)\cosh(p_1\bar{\delta})\,\mathrm{sech}(p_1)\sinh(\kappa H(-1 + \bar{\delta})) + p_1{}^3\epsilon_R\sinh(p_1\bar{\delta})\,\mathrm{sech}(p_1)\cosh(\kappa H(-1 + \bar{\delta}))} \\[4mm] Q_2 = \dfrac{\bar{\sigma}p_1\cosh(p_1\bar{\delta}) + q_1\epsilon_R\sinh(p_1\bar{\delta})}{\epsilon_R p_1{}^2\cosh(\kappa H(-1 + \bar{\delta}))\sinh(p_1\bar{\delta}) - p_1(\kappa H)\sinh(\kappa H(-1 + \bar{\delta}))\cosh(p_1\bar{\delta})} \end{cases} \qquad \text{(C.4)}$$

Within the Debye–Hückel electrostatic framework, the oscillatory EOF velocity may be deduced as follows

$$\bar{u}_0(\bar{y}) = \begin{cases} C_1\cosh(m_1\bar{y}) + C_2\sinh(m_1\bar{y}) + (m_1 m_2)^2\left[\left\{\dfrac{Q_1}{\cosh(p_1)(p_1{}^2 - m_1{}^2)}\right\}\right. & -1 < \bar{y} \leq -1 + \bar{\delta} \\[4mm] \left.\times\{\cosh(p_1(\bar{y} + 1)) - \cosh(m_1(\bar{y} + 1))\} + \left(\dfrac{2q_1}{p_1{}^2 m_1{}^2}\right)\sinh(m_1(\bar{y} + 1))\right] + m_2{}^2\bar{\psi}(\bar{y}); \\[4mm] C_3\cosh(m_3\bar{y}) + C_4\sinh(m_3\bar{y}) + \dfrac{m_3 Q_2}{(\kappa H)^2 - m_3{}^2}\left[m_3\cosh(\kappa H\bar{y}) - (\kappa H)\sinh(\kappa H(-1 + \bar{\delta}))\right. & -1 + \bar{\delta} < \bar{y} \leq 0 \\[4mm] \left.\times\sinh(m_3(\bar{y} + 1 - \bar{\delta})) - m_3\cosh(\kappa H(-1 + \bar{\delta}))\cosh(m_3(\bar{y} + 1 - \bar{\delta}))\right] + \bar{\psi}(\bar{y}); \end{cases} \qquad \text{(C.5)}$$
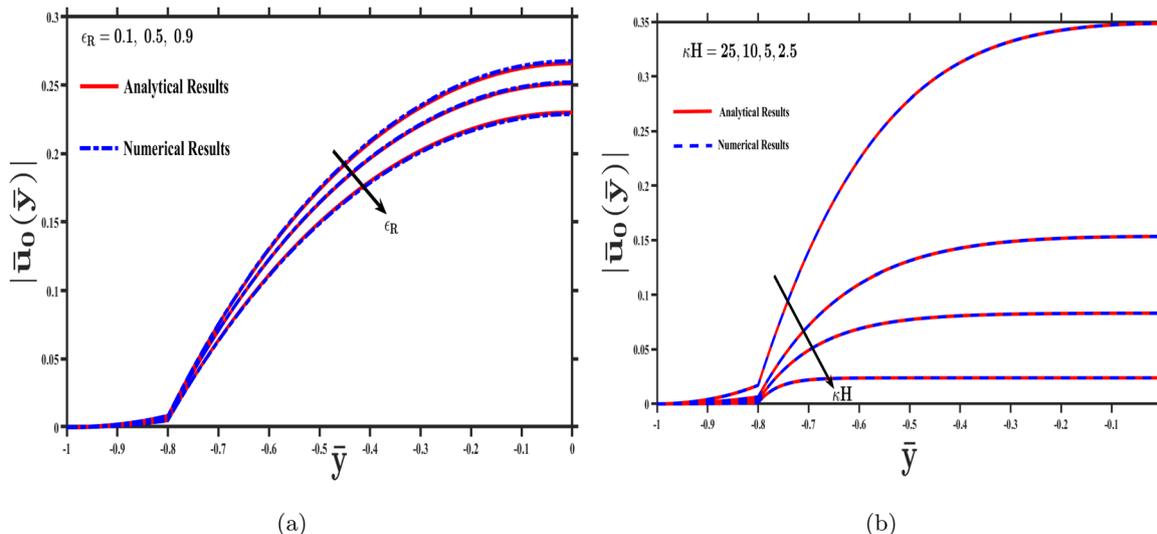
(a)

(b)

Fig. 14 In Fig. (a) and (b) we have shown the scaled velocity amplitude $|\bar{u}_0(\bar{y})|$ as a function of $\bar{y}$ for various values of ϵ_R (= 0.1, 0.5, and 0.9) with fixed $\kappa H = 2.5$; and various values of κH (= 2.5, 5, 10, and 25) with fixed $\epsilon_R = 0.1$. Other model parameters are $H = 25$ nm, $\delta = 5$ nm, $N_0 = 1$ mM, $\rho_R = 1.35$, $\eta_R = 2.54$, $\bar{\sigma} = 1$ and $\bar{\omega} = 10$, respectively.

The above expression for the velocity field involves various constants, *e.g.* C_i (i = 1, 2, 3, 4); m_i (i = 1, 2, 3), which are summarized in relation (A.1) appearing in the main MS. In order to validate the numerical results deduced in this present study, we have further shown the comparison for the EDL potential and the axial velocity in Fig. 14.

In Fig. 14a and b, we have shown the scaled velocity amplitude $|\bar{u}_0(\bar{y})|$ for various choices of ϵ_R and κH. The model parameters are indicated in the figure caption and they are chosen in such a way that the Debye–Hückel limit for EDL potential holds good. The deduced theoretical results are shown by solid lines and numerical results are further included by dashed lines. We have detailed the methods to deduce the numerical results for velocity amplitude in the main article. We observe a close agreement in the numerical results with the analytical results deduced in this section. It is noteworthy to mention that we may have a discrepancy in the numerical results with the analytical results presented in this section. The reason is the results presented in Appendix-C is valid only for low charge limits. Thus, for the case when the system charge is moderate to high, we need to use either semi-analytical results presented in Appendix-B or the complete numerical solution for electrostatic potential and hence the velocity amplitude.

Appendix-D Analytical results for several quantities associated with solute dispersion deduced under the Debye–Hückel electrostatic framework with $\omega \to 0$

The electroosmotic velocity distribution under Debye–Hückel approximation and externally applied electric field with $\omega \to 0$ may be written in the scaled form as follows

$$\bar{u}_0(\bar{y}) = \begin{cases} \dfrac{\epsilon_R Q_1}{\eta_R \cosh(p_1)}\{\cosh(p_1(\bar{y}+1)) - 1\}; & -1 < \bar{y} \leq -1 + \bar{\delta} \\ Q_2\{\cosh(\kappa H \bar{y}) + Q_3\}; & -1 + \bar{\delta} < \bar{y} \leq 0 \end{cases}$$
(D.1)

where Q_1, Q_2 are defined in (C.4) and Q_3 is defined as follows

$$Q_3 = -\frac{\epsilon_R}{\eta_R}\cosh(\kappa H) + \cosh(\kappa H(-1 + \bar{\delta}))\left\{\frac{\epsilon_R}{\eta_R} - 1\right\}$$
(D.2)

Using the expression of $\bar{u}_0(\bar{y})$, we may find the explicit analytical expression for cross-sectional mean fluid velocity $\bar{u}_m$, given as

$$\begin{aligned}\bar{u}_m &= \frac{\epsilon_R Q_1}{\eta_R \cosh(p_1)}\left[\frac{\sinh(p_1\bar{\delta})}{p_1} - \bar{\delta}\right] \\ &+ Q_2\left[-\frac{\sinh(\kappa H(-1 + \bar{\delta}))}{\kappa H} + Q_3(1 - \bar{\delta})\right]\end{aligned}$$
(D.3)

Now under the Debye–Hückel framework and externally applied electric field with $\omega \to 0$, the reduced form of the governing equation for $F(\bar{y})$ associated with dispersion process indicated earlier can be rewritten as

$$F''(\bar{y}) = \bar{u}_0(\bar{y}) - \bar{u}_m$$
(D.4)

In order to solve the function $F(\bar{y})$, the required conditions are given below

$$\left.\frac{\mathrm{d}F}{\mathrm{d}\bar{y}}\right|_{\bar{y}=-1} = 0$$
(D.5a)

$$\int_{-1}^{0} F(\bar{y})\mathrm{d}\bar{y} = 0$$
(D.5b)

Note that for applied electric field with $\omega \to 0$, the dispersion coefficient is free form time. We further denote the dispersion coefficient $K(\bar{t})$ as K_{eff}. Thus, for $\omega \to 0$, the dispersion coefficient K_{eff} may be deduced from (35), as follows

$$K_{eff} = \frac{1}{\mathrm{Pe}^2} - \int_{-1}^{0}(\bar{u}_0(\bar{y}) - \bar{u}_m)F(\bar{y})\mathrm{d}\bar{y}$$
(D.6)

Solving $F(\bar{y})$, the relation (D.6) may be rewritten as follows

$$K_{\text{eff}} = \frac{1}{\text{Pe}^2} + \int_{-1}^{0} [G(\bar{y})]^2 \, d\bar{y} \qquad \text{(D.7)}$$

where

$$G(\bar{y}) = \int_{-1}^{\bar{y}} (\bar{u}_0(\bar{y}) - \bar{u}_{\text{m}}) d\bar{y} = \begin{cases} \dfrac{\epsilon_R Q_1}{\eta_R \cosh(p_1)} \left[\dfrac{\sinh(p_1(\bar{y}+1))}{p_1} - (\bar{y}+1) \right] - \bar{u}_{\text{m}}(\bar{y}+1); & -1 < \bar{y} \le -1 + \bar{\delta} \\[3mm] Q_4 + Q_2 \left[\dfrac{\sinh(\kappa H \bar{y}) - \sinh(\kappa H(-1+\bar{\delta}))}{\kappa H} + Q_3(\bar{y}+1-\bar{\delta}) \right] - \bar{u}_{\text{m}}(\bar{y}+1-\bar{\delta}); & -1+\bar{\delta} < \bar{y} \le 0 \end{cases}$$

$$\text{(D.8)}$$

The expression $G(\bar{y})$ involves Q_i (1, 2, 3, 4). Note that Q_i (i = 1, 2, 3) are defined earlier and Q_4 is defined as follows

$$Q_4 = \frac{\epsilon_R Q_1}{\eta_R} \left[\frac{\sinh(p_1 \bar{\delta})}{p_1} - \bar{\delta} \right] - \bar{u}_{\text{m}} \bar{\delta} \qquad \text{(D.9)}$$
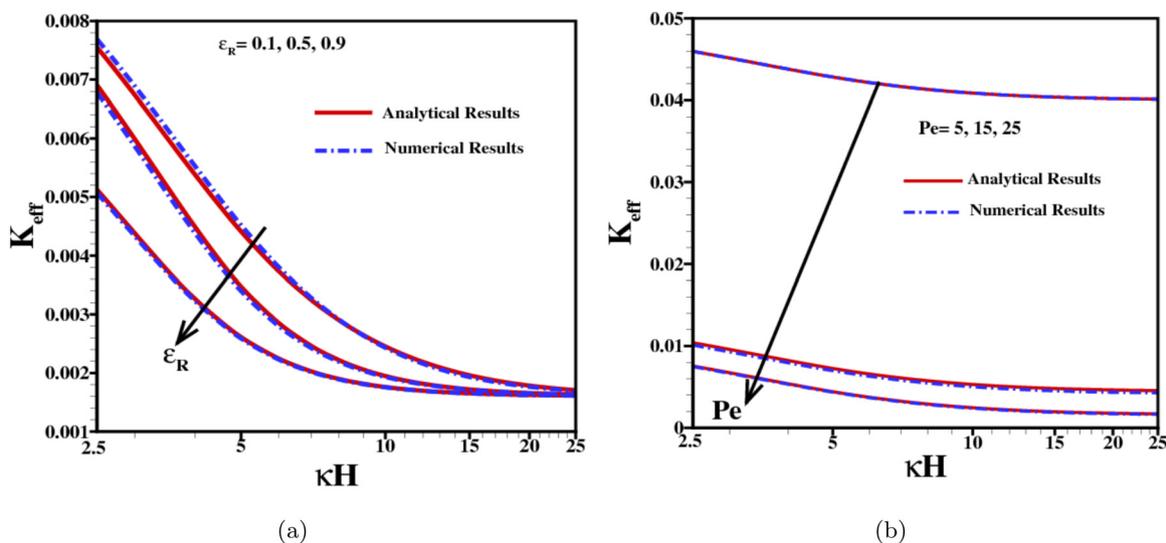

(a) (b)

Fig. 15 The dispersion coefficient K_{eff} is shown as a function of κH for various values of (a) ϵ_R (= 0.1, 0.5, and 0.9) with fixed Pe = 25 and (b) Pe (= 5, 15, and 25) with fixed $\epsilon_R = 0.1$. Other model parameters are H = 25 nm, δ = 5 nm, N_0 = 1 mM, $\rho_R = 1.35$, $\eta_R = 2.54$, $\bar{\sigma} = 1$ and $\bar{L} = 0.1$, respectively.

(a) (b)
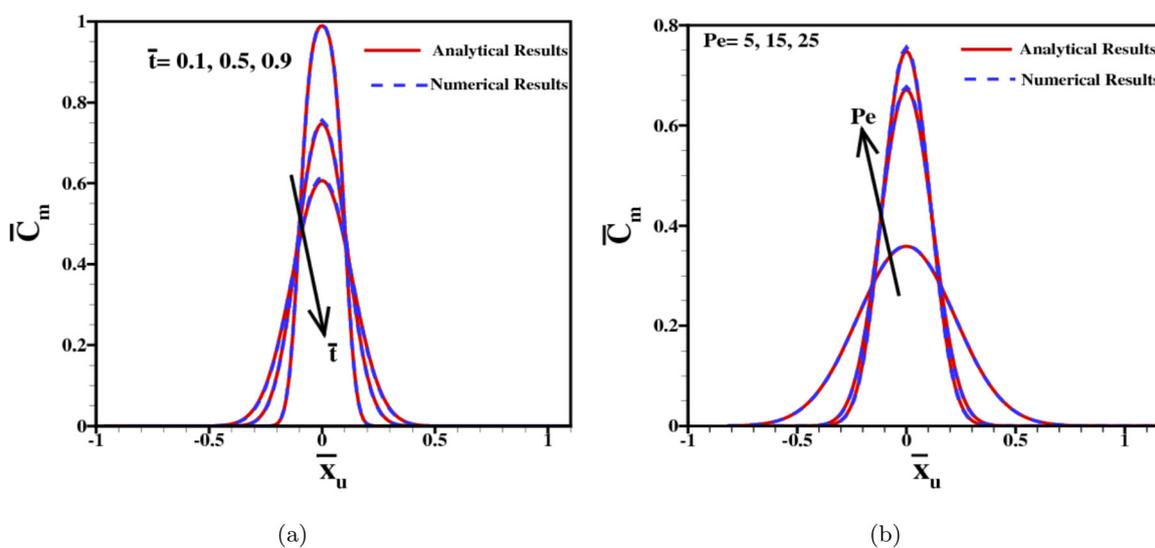
Fig. 16 The cross-sectional averaged $\bar{C}_{\text{m}}$ is shown for various values of (a) $\bar{t}$ (= 0.1, 0.5, and 0.9) with fixed Pe = 25 and (b) Péclet numbers Pe (= 5, 15, and 25) at time $\bar{t}$ = 0.5. The results are shown here considering dielectric liquid which surrounds the electrolytic solution as oily organic solvent cyclohexyl bromide (CHB) with fixed values of other model parameters, e.g., H = 25 nm, κ^{-1} = 10 nm, $\bar{\sigma}$ = 1 and r = 3.3 Å.

Substituting (D.8) into (D.7) yields the analytical expression of K_{eff}, given as

$$
\begin{aligned}
K_{eff} &= \frac{1}{Pe^2} + \frac{Q_5^2}{4p_1^3}S_1 + \frac{(Q_5 + \bar{u}_m)^2\bar{\delta}^3}{3} - \frac{2Q_5(Q_5 + \bar{u}_m)}{p_1^3}S_2 \\
&+ Q_6^2(1 - \bar{\delta}) + \frac{Q_2^2}{4(\kappa H)^3}S_3 \\
&+ \frac{2Q_2Q_6}{(\kappa H)^2}S_4 + \frac{2Q_2(Q_2Q_3 - \bar{u}_m)}{(\kappa H)^3}S_5 \\
&+ (Q_2Q_3 - \bar{u}_m)(1 - \bar{\delta})^2 S_6
\end{aligned}
$$

(D.10)

where the constants involved in the above relation (D.10) are given below

$$
\begin{cases}
Q_5 = \dfrac{\epsilon_R Q_1}{\eta_R \cosh(p_1)} \\[2mm]
Q_6 = Q_4 - \dfrac{Q_2 \sinh(\kappa H(-1 + \bar{\delta}))}{\kappa H} \\[2mm]
S_1 = -2p_1\bar{\delta} + \sinh(2p_1\bar{\delta}) \\[2mm]
S_2 = (p_1\bar{\delta})\cosh(p_1\bar{\delta}) - \sinh(p_1\bar{\delta}) \\[2mm]
S_3 = 2\kappa H(-1 + \bar{\delta}) - \sinh(2\kappa H(-1 + \bar{\delta})) \\[2mm]
S_4 = 1 - \cosh(\kappa H(-1 + \bar{\delta})) \\[2mm]
S_5 = \kappa H(1 - \bar{\delta}) + \sinh(\kappa H(-1 + \bar{\delta})) \\[2mm]
S_6 = Q_6 + \dfrac{(Q_2Q_3 - \bar{u}_m)(1 - \bar{\delta})}{3}
\end{cases}
$$

(D.11)
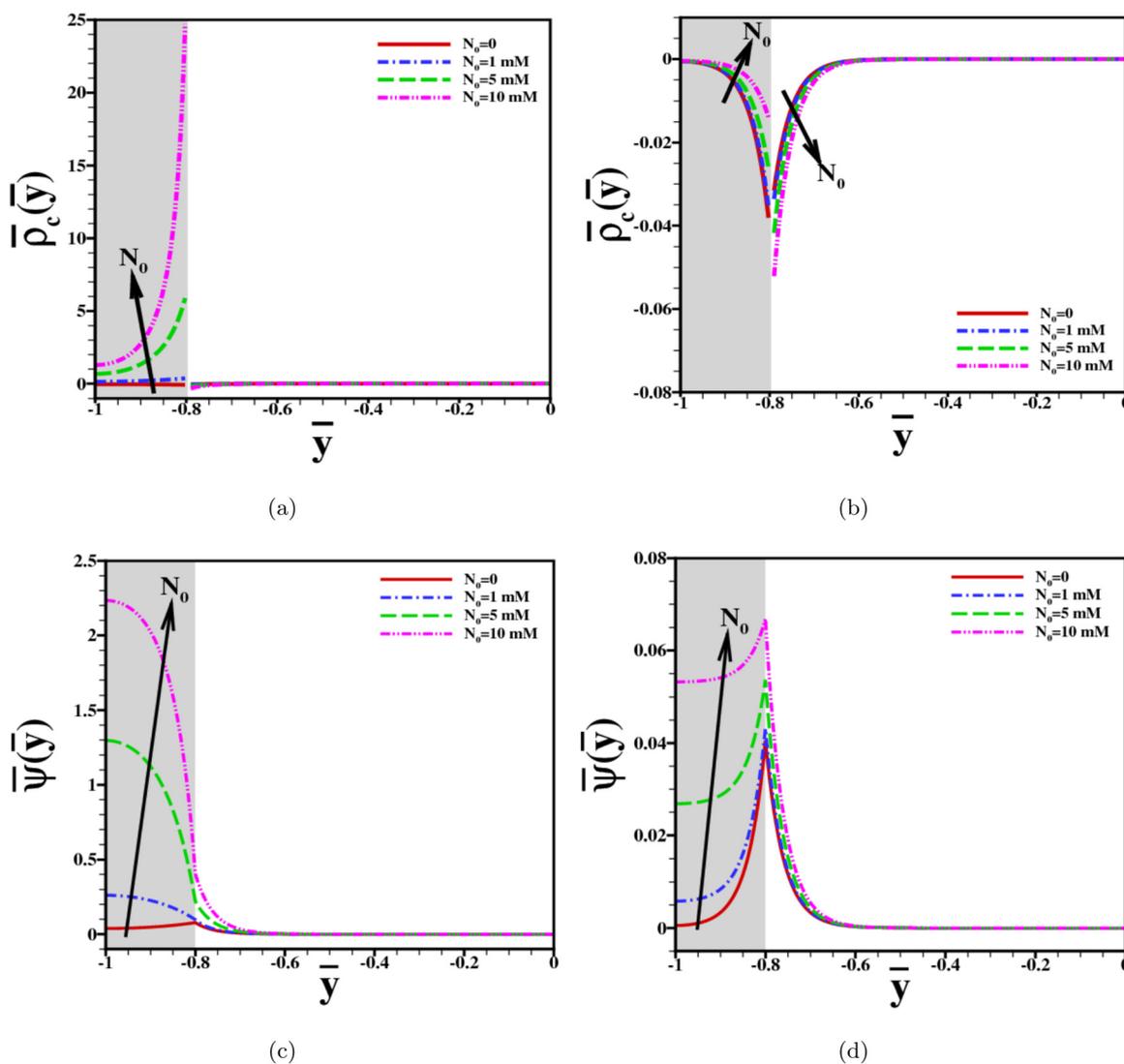
Fig. 17 Charge distribution of mobile ions $\bar{\rho}_c(\bar{y})$ (in the scaled form) and scaled potential distributions ($\bar{\psi}(\bar{y})$) are shown as a function of scaled spatial coordinate $\bar{y}$ for various values of N_0 (0, 1 mM, 5 mM, and 10 mM). In (a) and (c) we consider $\epsilon_R = 0.1$ and in (b) and (d) the value of dielectric permitivity ratio $\epsilon_R = 1$. Other model parameters are $H = 25$ nm, $\delta = 5$ nm, $\kappa H = 25$, $\bar{\sigma} = 2$, and $r = 3.3$ Å, respectively.

Under the limit of $\omega \to 0$, the governing equation for the cross sectional average concentration distribution $\bar{C}_m(\bar{x}_u, \bar{t})$ may be written as

$$\frac{\partial \bar{C}_m}{\partial \bar{t}} = K_{eff} \frac{\partial^2 \bar{C}_m}{\partial \bar{x}_u^2} \tag{D.12}$$

Solving eqn (D.12) subject to the initial condition (21) and boundary conditions (22a) and (22b), we may deduce the analytical expression of $\bar{C}_m(\bar{x}_u, \bar{t})$ as given below

$$\bar{C}_m(\bar{x}_u, \bar{t}) = \frac{1}{2}\left\{ \text{erf}\left(\frac{\bar{x}_u + \bar{L}}{2\sqrt{K_{eff}\bar{t}}}\right) - \text{erf}\left(\frac{\bar{x}_u - \bar{L}}{2\sqrt{K_{eff}\bar{t}}}\right) \right\} \tag{D.13}$$

In order to validate the numerical results for the solute dispersion process, we have shown the comparison of the numerically obtained effective dispersion coefficient and the cross-sectional averaged concentration in Fig. 15 and 16, respectively. The effective dispersion coefficient is shown as a function of κH for various choices of ϵ_R (Fig. 15a) and Pe (Fig. 15b). The time evolution of cross-sectional averaged solute concentration $\bar{C}_m$ is shown in Fig. 16a. We have further shown the results for $\bar{C}_m$ in Fig. 16b for various choices of Pe with fixed channel height. From all the results, it is clear that the numerical results are in close agreement in with the theoretical results deduced in this section.

Appendix-E: impact of the concentration of mobile ions N_0 on the overall charge distribution and electrostatic potential

Here we have shown the impact of concentration N_0 of additional ions within the surrounding liquid layer on the overall charge distribution (Fig. 17a and b) and electrostatic potential (Fig. 17c and d). We denote the overall charge density (in the scaled form) as $\bar{\rho}_c(\bar{y})$, which indicates the scaled form of $\rho_d(y)$ within the dielectric liquid layer and $\rho_e(y)$ within the electrolyte medium. The results are presented for two different values of ϵ_R (say, $\epsilon_R = 0.1$ and $\epsilon_R = 1$). When the permitivity ratio is far smaller than 1, say $\epsilon_R = 0.1$, the impact of the ion partitioning effect is prominent, however the ion partitioning effect is absent for $\epsilon_R = 1$. Thus, for $\epsilon_R = 0.1$, the penetration of the counterion across the dielectric liquid layer is less and leads to a higher value of net charge density within the liquid layer. As a result the magnitude in electrostatic potential is high, which in turn leads to a large value in electric driving force that leads to fluid motion. On the other hand, for $\epsilon_R = 1$, the accumulation of counterions within the dielectric liquid layer is sufficiently high and leads to a significant reduction in the overall charge distribution and hence a lower magnitude in the electrostatic potential.

Acknowledgements

References

1 H. A. Stone, A. D. Stroock and A. Ajdari, Engineering flows in small devices: microfluidics toward a lab-on-a-chip, *Annu. Rev. Fluid Mech.*, 2004, **36**(1), 381–411.

2 M. H. Oddy, J. G. Santiago and J. C. Mikkelsen, Electro-kinetic Instability Micromixing, *Anal. Chem.*, 2001, **73**(24), 5822–5832.

3 M. T. Kreutzer, A. Günther and K. F. Jensen, Sample Dispersion for Segmented Flow in Microchannels with Rectangular Cross Section, *Anal. Chem.*, 2008, **80**(5), 1558–1567.

4 G. Taylor, Dispersion of Soluble Matter in Solvent Flowing Slowly through a Tube, *Proc. R. Soc. London, Ser. A*, 1953, **219**(1137), 186–203.

5 R. Aris, On the Dispersion of a Solute in a Fluid Flowing through a Tube, *Proc. R. Soc. London, Ser. A*, 1956, **235**(1200), 67–77.

6 R. Aris, On the Dispersion of a Solute in Pulsating Flow Through a Tube, *Proc. R. Soc. London, Ser. A*, 1960, **259**(1298), 370–376.

7 S. Latunde-Dada, R. Bott, K. Hampton and O. I. Leszczyszyn, Application of the Exact Dispersion Solution to the Analysis of Solutes beyond the Limits of Taylor Dispersion, *Anal. Chem.*, 2015, **87**(15), 8021–8025.

8 V. Ananthakrishnan, W. N. Gill and A. J. Barduhn, Laminar dispersion in capillaries: Part I. Mathematical analysis, *AIChE J.*, 1965, **11**(6), 1063–1072.

9 W. N. Gill and R. Sankarasubramanian, Exact Analysis of Unsteady Convective Diffusion, *Proc. R. Soc. London, Ser. A*, 1970, **316**(1526), 341–350.

10 P. C. Fife and K. R. K. Nicholes, Dispersion in Flow Through Small Tubes, *Proc. R. Soc. London, Ser. A*, 1975, **344**(136), 131–145.

11 B. S. Mazumder and S. K. Das, Effect of boundary reaction on solute dispersion in pulsatile flow through a tube, *J. Fluid Mech.*, 1992, **239**(1), 523.

12 C.-O. Ng and T. L. Yip, Effects of kinetic sorptive exchange on solute transport in open-channel flow, *J. Fluid Mech.*, 2001, **446**, 321–345.

13 C.-O. Ng, Dispersion in steady and oscillatory flows through a tube with reversible and irreversible wall reactions, *Proc. R. Soc. London, Ser. A*, 2005, **462**(2066), 481–515.

14 S. Paul and B. S. Mazumder, Dispersion in unsteady Couette-Poiseuille flows, *Int. J. Eng. Sci.*, 2008, **46**(12), 1203–1217.

15 T. Karmakar, S. Barik and G. P. Raja Sekhar, Multi-scale analysis of concentration distribution in unsteady Couette-Poiseuille flows through a porous channel, *Proc. R. Soc. London, Ser. A*, 2023, **479**(2269), 20220494.

16 R. F. Probstein, *Physicochemical Hydrodynamics*, Wiley, New York, 2nd edn, 1994, pp. 53–164.

17 C.-O. Ng and Q. Zhou, Dispersion due to electroosmotic flow in a circular microchannel with slowly varying wall potential and hydrodynamic slippage, *Phys. Fluids*, 2012, **24**(11), 112002.

18 H. Stefan and R. Zengerle, Microfluidic platforms for lab-on-a-chip applications, *Lab Chip*, 2007, **7**(9), 1094–1110.

19 V. K. Kermani, M. Madadelahi, S. N. Ashrafizadeh, L. Kulinsky, S. O. Martinez-Chapa and M. J. Madou, Electrified lab on disc systems: a comprehensive review on electrokinetic applications, *Biosens. Bioelectron.*, 2022, **214**, 114381.

20 M. Khatibi and S. N. AshrafizadehIon, Transport in Intelligent Nanochannels: A Comparative Analysis of the Role of Electric Field, *Anal. Chem.*, 2023, **95**(49), 18188–18198.

21 V. Hoshyargar, S. N. Ashrafizadeh and A. Sadeghi, Drastic alteration of diffusioosmosis due to steric effects, *Phys. Chem. Chem. Phys.*, 2015, **17**(43), 29193–29200.

22 S. N. Ashrafizadeh, M. Zare and M. Khatibi, A Comprehensive Review of Pinch Flow Fractionation in Microfluidics: From Principles to Practical Applications, *Chem. Eng. Process.*, 2024, 110087.

23 A. Alinezhad, M. Khatibi and S. N. Ashrafizadeh, Impact of surface charge density modulation on ion transport in heterogeneous nanochannels, *Sci. Rep.*, 2024, **14**, 18409.

24 M. Khatibi, A. Aminnia and S. N. Ashrafizadeh, The role of ionic concentration polarization on the behavior of nanofluidic membranes, *Chem. Eng. Process.*, 2024, **202**, 109849.

25 S. Levine, J. R. Marriott, G. Neale and N. Epstein, Theory of electrokinetic flow in fine cylindrical capillaries at high zeta-potentials, *J. Colloid Interface Sci.*, 1975, **52**(1), 136–149.

26 M. Martin and G. Guiochon, Axial dispersion in open-tubular capillary liquid chromatography with electroosmotic flow, *Anal. Chem.*, 1984, **56**(4), 614–620.

27 S. K. Griffiths and R. H. Nilson, Hydrodynamic Dispersion of a Neutral Nonreacting Solute in Electroosmotic Flow, *Anal. Chem.*, 1999, **71**(24), 5522–5529.

28 S. K. Griffiths and R. H. Nilson, Electroosmotic Fluid Motion and Late-Time Solute Transport for Large Zeta Potentials, *Anal. Chem.*, 2000, **72**(20), 4767–4777.

29 D. Dutta, Electrokinetic Transport of Charged Samples through Rectangular Channels with Small Zeta Potentials, *Anal. Chem.*, 2008, **80**(12), 4723–4730.

30 V. Hoshyargar, M. Talebi, S. N. Ashrafizadeh and A. Sadeghi, Hydrodynamic dispersion by electroosmotic flow of viscoelastic fluids within a slit microchannel, *Microfluid. Nanofluid.*, 2017, **22**(1), 1–15.

31 A. E. Herr, J. I. Molho, J. G. Santiago, M. G. Mungal, T. W. Kenny and M. G. Garguilo, Electroosmotic Capillary Flow with Nonuniform Zeta Potential, *Anal. Chem.*, 2000, **72**(5), 1053–1057.

32 S. Ghosal, Band Broadening in a Microcapillary with a Stepwise Change in the ζ-potential, *Anal. Chem.*, 2002, **74**(16), 4198–4203.

33 E. K. Zholkovskij, J. H. Masliyah and A. E. Yaroshchuk, Broadening of neutral analyte band in electroosmotic flow through slit channel with different ζ-potentials of the walls, *Microfluid. Nanofluidics*, 2012, **15**(1), 35–47.

34 J. C. Arcos, F. Méndez, E. G. Bautista and O. Bautista, Dispersion coefficient in an electro-osmotic flow of a viscoelastic fluid through a microchannel with a slowly varying wall zeta potential, *J. Fluid Mech.*, 2018, **839**, 348–386.

35 A. Ramos, H. Morgan, N. G. Green and A. Castellanos, Ac electrokinetics: a review of forces in microelectrode structures, *J. Phys. D: Appl. Phys.*, 1998, **31**(18), 2338–2353.

36 J. Experton, X. Wu and C. Martin, From Ion Current to Electroosmotic Flow Rectification in Asymmetric Nanopore Membranes, *Nanomaterials*, 2017, **7**(12), 445.

37 M. R. Hossan, D. Dutta, N. Islam and P. Dutta, Review: electric field driven pumping in microfluidic device, *Electrophoresis*, 2018, **39**, 702–731.

38 S. Talapatra and S. Chakraborty, Double layer overlap in ac electroosmosis, *Eur. J. Mech. B Fluids*, 2008, **27**(3), 297–308.

39 M. Selmi and H. Belmabrouk, AC Electroosmosis Effect on Microfluidic Heterogeneous Immunoassay Efficiency, *Micromachines*, 2020, **11**(4), 342.

40 P. Dutta and A. Beskok, Analytical Solution of Time Periodic Electroosmotic Flows: Analogies to Stokes Second Problem, *Anal. Chem.*, 2001, **73**(21), 5097–5102.

41 X. Xuan and D. Li, Electroosmotic flow in microchannels with arbitrary geometry and arbitrary distribution of wall charge, *J. Colloid Interface Sci.*, 2005, **289**(1), 291–303.

42 W.-J. Luo, Transient electroosmotic flow induced by AC electric field in micro-channel with patchwise surface heterogeneities, *J. Colloid Interface Sci.*, 2006, **295**(2), 551–561.

43 S. Chakraborty, Augmentation of peristaltic microflows through electro-osmotic mechanisms, *J. Phys. D: Appl. Phys.*, 2006, **39**(24), 5356–5363.

44 S. Bhattacharyya and A. K. Nayak, Time periodic electroosmotic transport in a charged micro/nano-channel, *Colloids Surf., A*, 2008, **325**(3), 152–159.

45 Q. Liu, Y. Jian and L. Yang, Time periodic electroosmotic flow of the generalized Maxwell fluids between two micro-parallel plates, *J. Non-Newtonian Fluid Mech.*, 2011, **166**(9–10), 478–486.

46 A. J. Moghadam, Thermal characteristics of time-periodic electroosmotic flow in a circular microchannel, *Heat Mass Transfer*, 2015, **51**(10), 1461–1473.

47 A. Haque, A. K. Nayak, B. Weigand and A. Banerjee, Time dependent electroosmotic flow in micro-channels with variable wall slip zones, *Ind. Eng. Chem. Res.*, 2019, **59**(2), 942–955.

48 H. F. Huang and C. L. Lai, Enhancement of mass transport and separation of species by oscillatory electroosmotic flows, *Proc. R. Soc. London, Ser. A*, 2006, **462**(2071), 2017–2038.

49 G. Ramon, Y. Agnon and C. Dosoretz, Solute dispersion in oscillating electro-osmotic flow with boundary mass exchange, *Microfluid. Nanofluidics*, 2010, **10**(1), 97–106.

50 S. Paul and C.-O. Ng, Dispersion in electroosmotic flow generated by oscillatory electric field interacting with oscillatory wall potentials, *Microfluid. Nanofluidics*, 2011, **12**(1–4), 237–256.

51 C. Teodoro, O. Bautista and F. Mendez, Mass transport and separation of species in an oscillating electroosmotic flow

caused by distinct periodic electric fields, *Phys. Scr.*, 2019, **94**, 115012.

52 H. Li and Y. Jian, Dispersion for periodic electro-osmotic flow of Maxwell fluid through a microtube, *Int. J. Heat Mass Transfer*, 2017, **115**, 703–713.

53 A. Kumar and S. De, Effect of AC electric field in mass transport of a neutral solute in a microtube with porous wall, *Chem. Eng. Sci.*, 2024, **288**, 119832.

54 F. Li and Y. Jian, Solute dispersion generated by alternating current electric field through polyelectrolyte-grafted nanochannel with interfacial slip, *Int. J. Heat Mass Transfer*, 2019, **141**, 1066–1077.

55 M. Reshadi and M. H. Saidi, Tuning the dispersion of reactive solute by steady and oscillatory electroosmotic-Poiseuille flows in polyelectrolyte-grafted micro/nano-tubes, *J. Fluid Mech.*, 2019, **880**, 73–112.

56 V. Hoshyargar, A. Khorami, S. N. Ashrafizadeh and A. Sadeghi, Solute dispersion by electroosmotic flow through soft microchannels, *Sens. Actuators, B*, 2018, **255**, 3585–3600.

57 B. Saha, S. Chowdhury, S. Sarkar and P. P. Gopmandal, Electroosmotic flow modulation and dispersion of uncharged solutes in soft nanochannel, *Soft Matter*, 2024, **20**(32), 6458–6489.

58 S. Debesset, C. J. Hayden, C. Dalton, J. C. T. Eijkel and A. Manz, An AC electroosmotic micropump for circular chromatographic applications, *Lab Chip*, 2004, **4**(4), 396.

59 G. Yan, S. K. Li and W. I. Higuchi, Evaluation of constant current alternating current iontophoresis for transdermal drug delivery, *J. Controlled Release*, 2005, **110**(1), 141–150.

60 H. Gaikwad, G. Kumar and P. Mondal, Efficient Electro-osmotic Mixing in a Narrow-Fluidic Channel: The Role of a Patterned Soft Layer, *Soft Matter*, 2020, **27**, 1–29.

61 J. Song, C.-O. Ng and W.-K. A. Law, Dispersion in oscillatory electro-osmotic flow through a parallel-plate channel with kinetic sorptive exchange at walls, *J. Hydrodyn., Ser. B*, 2014, **26**(3), 363–373.

62 I. Medina, M. Toledo, F. Méndez and O. Bautista, Pulsatile electroosmotic flow in a microchannel with asymmetric wall zeta potentials and its effect on mass transport enhancement and mixing, *Chem. Eng. Sci.*, 2018, **184**, 259–272.

63 M. Karimzadeh, Z. Seifollahi, M. Khatibi and S. N. Ashrafizadeh, Impacts of the shape of soft nanochannels on their ion selectivity and current rectification, *Electrochim. Acta*, 2021, **399**, 139376.

64 H. Dartoomi, M. Khatibi and S. N. Ashrafizadeh, Importance of nanochannels shape on blue energy generation in soft nanochannels, *Electrochim. Acta*, 2022, **431**, 141175.

65 H. Dartoomi, M. Khatibi and S. N. Ashrafizadeh, Nanofluidic Membranes to Address the Challenges of Salinity Gradient Energy Harvesting: Roles of Nanochannel Geometry and Bipolar Soft Layer, *Langmuir*, 2022, **38**(33), 10313–10330.

66 M. Karimzadeh, M. Khatibi, S. N. Ashrafizadeh and P. K. Mondal, Blue energy generation by the temperaturedependent

properties in funnel-shaped soft nanochannels, *Softmatter*, 2022, **24**, 20303.

67 D. Jafari, M. Khatibi and S. N. Ashrafizadeh, Blue energy conversion utilizing smart ionic nanotransistors, *Electrochim. Acta*, 2024, **507**, 145186.

68 N. Qiao, Z. Zhang, A. Liu, W. Lu and C. Li, Ion current rectification in asymmetric nanochannels: effects of nanochannel shape and surface charge, *Int. J. Heat Mass Transfer*, 2023, **208**, 124038.

69 H. Dartoomi, M. Khatibi and S. N. Ashrafizadeh, Enhanced Ionic Current Rectification through Innovative Integration of Polyelectrolyte Bilayers and Charged-Wall Smart Nanochannels, *Anal. Chem.*, 2023, **95**(2), 1522–1531.

70 M. Karimzadeh, M. Khatibi and S. N. Ashrafizadeh, Boost ionic selectivity by coating bullet-shaped nanochannels with dense polyelectrolyte brushes, *Phys. Fluids*, 2022, **34**, 122008.

71 A. Alinezhad, M. Khatibi and S. N. Ashrafizadeh, Impact of asymmetry soft layers and ion partitioning on ionic current rectification in bipolar nanochannels, *J. Mol. Liq.*, 2022, **347**, 118324.

72 A. Alinezhad, M. Khatibi and S. N. Ashrafizadeh, Ionic transfer behavior of bipolar nanochannels resembling PNP nanotransistor, *Electrochim. Acta*, 2023, **460**, 142625.

73 R. Chein and B. Chung, Numerical study of ionic current rectification through non-uniformly charged micro/nanochannel systems, *J. Appl. Electrochem.*, 2013, **43**, 1197–1206.

74 Y. Gao, T. N. Wong, C. Yang and K. T. Ooi, Transient two-liquid electroosmotic flow with electric charges at the interface, *Colloids Surf., A*, 2005, **266**(1–3), 117–128.

75 C. Wang, Q. Gao and Y. Song, Electrokinetic Effect of a Two-Liquid Interface within a Slit Microchannel, *Langmuir*, 2023, **39**, 17529–17537.

76 L. Haiwang, T. N. Wong and N.-T. Nguyen, Time-dependent model of mixed electroosmotic/pressure-driven three immiscible fluids in a rectangular microchannel, *Int. J. Heat Mass Transfer*, 2010, **53**(4), 772–785.

77 J. Su, Y.-J. Jian, L. Chang and Q.-S. Li, Transient electro-osmotic and pressure driven flows of two-layer fluids through a slit microchannel, *Acta Mech. Sin.*, 2013, **29**(4), 534–542.

78 M. Mayur, S. Amiroudine, D. Lasseux and S. Chakraborty, Effect of interfacial Maxwell stress on time periodic electroosmotic flow in a thin liquid film with a flat interface, *Electrophoresis*, 2013, **35**(5), 670–680.

79 S. Mandal, U. Ghosh, A. Bandopadhyay and S. Chakraborty, Electro-osmosis of superimposed fluids in the presence of modulated charged surfaces in narrow confinements, *J. Fluid Mech.*, 2015, **776**, 390–429.

80 A. Navarkar, S. Amiroudine and E. A. Demekhin, On two-liquid AC electroosmotic system for thin films, *Electrophoresis*, 2016, **37**(5–6), 727–735.

81 S. Deng, T. Xiao and C. Liang, Analytical study of unsteady two-layer combined electroosmotic and pressure-driven flow through a cylindrical microchannel with slip-dependent zeta potential, *Chem. Eng. Sci.*, 2024, **283**, 119327.

82 H. Ohshima, K. Nomura, H. Kamaya and I. Ueda, Liquid membrane: equilibrium potential distribution across lipid monolayer-coated oil/water interface, *J. Colloid Interface Sci.*, 1985, **106**(2), 470–478.

83 P. Mahapatra, H. Ohshima and P. P. Gopmandal, Electrophoresis of Liquid-Layer Coated Particles: Impact of Ion Partitioning and Ion Steric Effects, *Langmuir*, 2021, **37**(38), 11316–11329.

84 S. J. Singer and G. L. Nicolson, The Fluid Mosaic Model of the Structure of Cell Membranes, *Science*, 1972, **175**(4023), 720–731.

85 H. G. L. Coster, The Double Fixed Charge Membrane, *Biophys. J.*, 1973, **13**(2), 133–142.

86 P. Goswami, S. De and P. P. Gopmandal, Streaming Potential and Associated Electrokinetic Effects through a Channel Filled with Electrolyte Solution Surrounded by a Layer of Immiscible and Dielectric Liquid, *Langmuir*, 2024, **40**(22), 11695–11712.

87 N. F. Carnahan and K. E. Starling, Equation of State for Nonattracting Rigid Spheres, *J. Chem. Phys.*, 1969, **51**(2), 635–636.

88 J. J. López-García, J. Horno and C. Grosse, Influence of steric interactions on the dielectric and electrokinetic properties in colloidal suspensions, *J. Colloid Interface Sci.*, 2015, **458**, 273–283.

89 H. Ohshima, A simple algorithm for the calculation of an approximate electrophoretic mobility of a spherical colloidal particle based on the modified Poisson-Boltzmann equation, *Colloid Polym. Sci.*, 2017, **295**(4), 543–548.

90 P. P. Gopmandal and H. Ohshima, Modulation of electroosmotic flow through electrolyte column surrounded by a dielectric oil layer, *Colloid Polym. Sci.*, 2017, **295**(7), 1141–1151.

91 H. Jing and S. Das, Electric double layer electrostatics of lipid-bilayer-encapsulated nanoparticles: toward a better understanding of protocell electrostatics, *Electrophoresis*, 2018, **39**(5–6), 752–759.

92 Z. Seifollahi and S. N. Ashrafizadeh, Effect of charge density distribution of polyelectrolyte layer on electroosmotic flow and ion selectivity in a conical soft nanochannel, *Chem. Eng. Sci.*, 2022, **261**, 117986.

93 A. Ganjizade, S. N. Ashrafizadeh and A. Sadeghi, Effect of ion partitioning on the electrostatics of soft particles with a volumetrically charged core, *Electrochem. Commun.*, 2017, **84**, 19–23.

94 A. Ganjizade, S. N. Ashrafizadeh and A. Sadeghi, Significant alteration in DNA electrophoretic translocation velocity through soft nanopores by ion partitioning, *Anal. Chim. Acta*, 2019, **1080**, 66–74.

95 M. Reshadi and M. H. Saidi, The role of ion partitioning in electrohydrodynamic characteristics of soft nanofluidics: inclusion of EDL overlap and steric effects, *Chem. Eng. Sci.*, 2018, **190**, 443–458.

96 J. N. Israelachvili, *Intermolecular and surface forces*, Academic Press, 3rd edn, 2011, pp. 273–277.

97 H. Ohshima, An approximate analytic solution to the modified Poisson–Boltzmann equation: effects of ionic size, *Colloid Polym. Sci.*, 2016, **294**(12), 2121–2125.

98 H. Ohshima, Theory of electrostatics and electrokinetics of soft particles, *Sci. Technol. Adv. Mater.*, 2009, **10**(6), 063001.

99 J. S. H. Lee, I. Barbulovic-Nad, Z. Wu, X. Xuan and D. Li, Electrokinetic flow in a free surface-guided microchannel, *J. Appl. Phys.*, 2006, **99**(5), 054905.

100 W. N. Gill, Analysis of axial dispersion with time variable flow, *Chem. Eng. Sci.*, 1967, **22**(7), 1013–1017.

101 M. E. Leunissen, J. Zwanikken, R. van Roij, P. M. Chaikin and A. van Blaaderen, Ion partitioning at the oil-water interface as a source of tunable electrostatic effects in emulsions with colloids, *Phys. Chem. Chem. Phys.*, 2007, **9**(48), 6405.

102 A. R. Kneller, D. G. Haywood and S. C. Jacobson, AC Electroosmotic Pumping in Nanofluidic Funnels, *Anal. Chem.*, 2016, **88**(12), 6390–6394.

103 A. J. Moghadam and P. Akbarzadeh, AC two-immiscible-fluid EOF in a microcapillary, *J. Braz. Soc. Mech. Sci. Eng.*, 2019, **41**, 194.

104 A. Sadeghi, Analytical solutions for mass transport in hydrodynamic focusing by considering different diffusivities for sample and sheath flows, *J. Fluid Mech.*, 2019, **862**, 517–551.

105 S. Vedel and H. Bruus, Transient Taylor-Aris dispersion for time-dependent flows in straight channels, *J. Fluid Mech.*, 2011, **691**, 95–122.

106 H. Li and Y. Jian, Dispersion for periodic electro-osmotic flow of Maxwell fluid through a microtube, *Int. J. Heat Mass Transfer*, 2017, **115**, 703–713.

107 A. Mukherjee and B. S. Mazumder, Dispersion of contaminant in oscillatory flows, *Acta Mech.*, 1988, **74**(1–4), 107–122.